

© Copyright [2010] American Meteorological Society (AMS). Permission to use figures, tables, and brief excerpts from this work in scientific and educational works is hereby granted provided that the source is acknowledged. Any use of material in this work that is determined to be “fair use” under Section 107 of the U.S. Copyright Act or that satisfies the conditions specified in Section 108 of the U.S. Copyright Act (17 USC §108, as revised by P.L. 94-553) does not require the AMS’s permission. Republication, systematic reproduction, posting in electronic form on servers, or other uses of this material, except as exempted by the above statement, requires written permission or a license from the AMS. Additional details are provided in the AMS Copyright Policy, available on the AMS Web site located at (<http://www.ametsoc.org/AMS>) or from the AMS at 617-227-2425 or [copyright@ametsoc.org](mailto:copyright@ametsoc.org).

An edited version of this paper was published by American Meteorological Society.

## Seasonal mixed layer heat balance of the southwestern tropical Indian Ocean

Gregory R. Foltz<sup>1</sup>, Jérôme Vialard<sup>2</sup>, Praveen Kumar B.<sup>3</sup>, and Michael J. McPhaden<sup>4</sup>

<sup>1</sup>University of Washington/Joint Institute for the Study of the Atmosphere and Ocean, Seattle, WA

<sup>2</sup>IRD/Laboratoire d'Océanographie Expérimentation et Approches Numériques, Paris, France

<sup>3</sup>National Institute of Oceanography/Physical Oceanography Division, Dona Paula, Goa, India

<sup>4</sup>NOAA/Pacific Marine Environmental Laboratory, Seattle, WA

Corresponding author: [gregory.foltz@noaa.gov](mailto:gregory.foltz@noaa.gov)

Revised for *Journal of Climate*

18 August 2009

# 1 Abstract

2 Sea surface temperature (SST) in the southwestern tropical Indian Ocean exerts a  
3 significant influence on global climate through its influence on the Indian summer  
4 monsoon and northern hemisphere atmospheric circulation. In this study measure-  
5 ments from a long-term moored buoy are used in conjunction with satellite, in situ,  
6 and atmospheric reanalysis data sets to analyze the seasonal mixed layer heat balance  
7 in the thermocline ridge region of the southwestern tropical Indian Ocean. This region  
8 is characterized by a shallow mean thermocline (90 m) and strong seasonal cycles of  
9 Ekman pumping and SST (seasonal ranges of  $-0.1$  to  $0.6$  m day<sup>-1</sup> and  $26^{\circ}\text{C}$  to  $29.5^{\circ}\text{C}$ ,  
10 respectively). It is found that surface heat fluxes and horizontal heat advection con-  
11 tribute significantly to the seasonal cycle of mixed layer heat storage. The net surface  
12 heat flux tends to warm the mixed layer throughout the year and is strongest during  
13 boreal fall and winter, when surface shortwave radiation is highest and latent heat loss  
14 is weakest. Horizontal heat advection provides warming during boreal summer and  
15 fall, when southwestward surface currents and horizontal SST gradients are strongest,  
16 and is close to zero during the remainder of the year. Vertical turbulent mixing, es-  
17 timated as a residual in the heat balance, also undergoes a significant seasonal cycle.  
18 Cooling from this term is strongest in boreal summer, when surface wind and buoyancy  
19 forcing are strongest, the thermocline ridge is shallow ( $<90$  m), and the mixed layer is  
20 deepening. These empirical results provide a framework for addressing intraseasonal  
21 and interannual climate variations, which are dynamically linked to the seasonal cycle,  
22 in the southwestern tropical Indian Ocean. They also provide a quantitative basis for  
23 assessing the accuracy of numerical ocean model simulations in the region.

# 24 1 Introduction

25 The southwestern tropical Indian Ocean is characterized by a pronounced thermocline  
26 ridge (the Seychelles-Chagos thermocline ridge (SCTR); Fig. 1). The SCTR is main-  
27 tained primarily by Ekman pumping associated with a northward weakening of the  
28 southeasterly trade winds. SST remains warm in the SCTR region ( $>26^{\circ}\text{C}$  throughout  
29 the year and  $28^{\circ}\text{C}$  in the annual mean) despite a shallow thermocline and annual mean  
30 upwelling. These conditions are typical of those found in other tropical convergence  
31 zones. For example, the thermocline depth and SST in the SCTR region are similar to  
32 those found in the Atlantic and central tropical Pacific intertropical convergence zones  
33 ( $2^{\circ}\text{N}$ – $8^{\circ}\text{N}$ ,  $20^{\circ}\text{W}$ – $45^{\circ}\text{W}$  and  $5^{\circ}\text{N}$ – $10^{\circ}\text{N}$ ,  $120^{\circ}\text{W}$ – $160^{\circ}\text{W}$ , respectively).

34 Because of high mean SSTs in the SCTR region, small perturbations can exert  
35 a strong influence on weather and climate on the surrounding continents. Interannual  
36 SST anomalies in the SCTR region affect rainfall in East Africa (Goddard and Graham  
37 1999; Black et al. 2003; Ummenhofer et al. 2009), the onset and strength of the Indian  
38 summer monsoon (Joseph et al. 1994; Vecchi and Harrison 2004; Annamalai et al.  
39 2005; Izumo et al. 2008), and ENSO teleconnections to the North Pacific (Annamalai  
40 et al. 2007). There are also strong intraseasonal fluctuations of SST in the SCTR  
41 region that are associated with the eastward-propagating Madden-Julian Oscillation  
42 (e. g., Duvel and Vialard 2007). Ocean dynamics seem to be responsible for most of  
43 the SST variability on interannual timescales (Murtugudde and Busalacchi 1999; Xie  
44 et al. 2002), while surface fluxes and entrainment appear to contribute significantly to  
45 intraseasonal SST variability (Vecchi and Harrison 2001; Saji et al. 2006; Duvel and  
46 Vialard 2007; Han et al. 2007; Vinayachandran and Saji 2008; Vialard et al. 2008).

47 Interannual and intraseasonal SST variability in the SCTR region is superimposed

48 on a pronounced seasonal cycle (Fig. 1a,b). Several previous studies have addressed the  
49 seasonal cycle in the SCTR region. Hermes and Reason (2008) used a regional ocean  
50 model to investigate the seasonal cycle in the SCTR region. They found that the net  
51 surface heat flux is balanced to a large extent by the sum of horizontal convergence and  
52 vertical diffusion. In their model the upper ocean heat content in the SCTR region  
53 is a small residual between these two larger terms and is characterized by a strong  
54 semiannual cycle. Using an ocean general circulation model, Yokoi et al. (2008) found  
55 a pronounced semiannual variation of upper ocean heat content (averaged from the  
56 surface to 100 m), in agreement with Hermes and Reason (2008). In their model, the  
57 seasonal cycle of heat content was driven mainly by a strong semiannual cycle of Ekman  
58 pumping, with weaker and out of phase contributions from horizontal advection and the  
59 net surface heat flux. They showed that the semiannual cycle of Ekman pumping is due  
60 to the interference between the curl and beta terms. Zhou et al. (2008) analyzed the  
61 mixed layer temperature balance in the SCTR region from an ocean general circulation  
62 model. During boreal summer they found that there is strong warming from horizontal  
63 advection that balances cooling from entrainment. As a result, the seasonal cycle  
64 of SST is driven primarily by the net surface heat flux. They also show that the  
65 seasonal cycle of Indonesian throughflow affects the vertical stratification and hence  
66 the seasonality of the entrainment heat flux.

67 The aforementioned studies suggest that surface heat fluxes, horizontal advec-  
68 tion, and entrainment play important roles in the upper ocean heat balance of the  
69 SCTR region. However, these studies are inconclusive regarding the causes of the sea-  
70 sonal cycle of SST. For example, Hermes and Reason (2008) and Yokoi et al. (2008)  
71 investigated seasonal variations in upper ocean heat content, but did not explicitly

72 address the causes of the strong seasonal cycle of SST. Zhou et al. (2008) analyzed the  
73 mixed layer temperature balance, but for a limited region ( $6^{\circ}\text{S}$ – $7^{\circ}\text{S}$ ,  $63^{\circ}\text{E}$ – $73^{\circ}\text{E}$ ). All  
74 three studies relied on output from numerical ocean models. In this study we analyze  
75 the mixed layer heat budget in the SCTR region from a combination of satellite and  
76 in situ data sets and simple one-dimensional diagnostic models, expanding on previous  
77 modeling studies.

## 78 **2 Data**

79 We use a combination of satellite and in situ data sets to analyze the mixed layer heat  
80 budget in the southwestern tropical Indian Ocean. Satellite and Argo data are used to  
81 examine the heat budget in the SCTR region during 2000–2008. Measurements from a  
82 buoy of the Research moored array for African-Asian-Australian monsoon analysis and  
83 prediction (RAMA; McPhaden et al. 2009) at  $8^{\circ}\text{S}$ ,  $67^{\circ}\text{E}$  complement the larger-scale  
84 analysis, providing direct measurements at a single location during 2007–2008.

### 85 **2.1 Satellite and Argo**

86 SST and rainfall are available from the Tropical Rainfall Measuring Mission (TRMM)  
87 Microwave/Imager (TMI) on a  $0.5^{\circ}\times 0.5^{\circ}\times 3$ -day grid from December 1997 to the  
88 present. We also use a combined TMI/AMSR-E SST data set on the same spatial grid  
89 for the time period June 2002 through the present. Surface wind velocity was obtained  
90 from the SeaWinds scatterometer onboard the QuikSCAT satellite on a  $0.25^{\circ}\times 0.25^{\circ}\times 3$ -  
91 day grid beginning July 1999. Monthly mean estimates of near-surface chlorophyll-a  
92 concentration from the Sea-viewing Wide Field-of-view Sensor (SeaWiFS) onboard the  
93 SeaStar satellite are used to calculate penetrative shortwave radiation. These data are  
94 available on a  $0.08^{\circ}\times 0.08^{\circ}$  grid for 1997–present.

95 The Coriolis Centre at IFREMER produces weekly three-dimensional analyses  
96 of temperature, salinity, and density based on Argo and other available mooring, XBT  
97 and CTD data. The analyses are produced using an optimal interpolation scheme with  
98 climatology used as a background (Gaillard et al. 2009). The data are available on a  
99 global grid with  $\sim 0.5^\circ$  horizontal resolution and vertical resolution of 5 to 20 m in the  
100 upper 300 m. We use the temperature, salinity and density analyses computed weekly  
101 to compute the mixed layer depth (MLD), isothermal layer depth (ILD), depth of the  
102  $20^\circ\text{C}$  isotherm, and temperature jump at the base of the mixed layer (these data sets  
103 are hereafter referred to as the “Coriolis” MLD, ILD, etc.). The MLD is computed  
104 using the criterion of a  $0.15 \text{ kg m}^{-3}$  density increase from the density at a depth of 5 m.  
105 The ILD is calculated using the temperature equivalent of a  $0.15 \text{ kg m}^{-3}$  increase from  
106 a depth of 5 m. The temperature jump at the base of the mixed layer ( $\Delta T$ ) is computed  
107 as the difference between the mean mixed layer temperature and the temperature 10  
108 m below the base of the mixed layer. For heat budget sensitivity tests, we also use  
109 a monthly gridded MLD product that is based on individual Argo temperature and  
110 salinity profiles (Clement de Boyer Montégut, personal communication, 2009). In this  
111 data set the MLD is defined using the criterion of a  $0.03 \text{ kg m}^{-3}$  density increase from  
112 a depth of 10 m. This smaller criterion was found to be optimal for estimating MLD  
113 from individual profiles (de Boyer Montégut et al. 2004).

114 We use two different estimates of horizontal velocity. The first calculates hori-  
115 zontal velocity averaged in the upper 30 m from the Ocean Surface Current Analysis  
116 – Realtime (OSCAR; Bonjean and Lagerloef 2002). This method uses satellite sea  
117 level, wind stress, and SST, together with a diagnostic model, to calculate velocity on  
118 a  $1^\circ \times 1^\circ \times 5$ -day grid for the time period 1993–2006. The second uses near-surface

119 velocity from satellite-tracked drifting buoys and is available as a monthly mean cli-  
120 matology on a  $1^\circ \times 1^\circ$  grid (Lumpkin and Garzoli 2005). The OSCAR product has  
121 the advantage of more complete spatial and temporal coverage than the drifter-based  
122 climatology because it uses satellite measurements, but has the disadvantage of not  
123 being constrained by direct velocity observations.

124 Two different net surface heat flux products are used in this study. For the first  
125 product (hereafter *Flux<sub>QuikSCAT</sub>*), latent and sensible heat fluxes are calculated with  
126 version 3.0 of the Coupled Ocean Atmosphere Response Experiment (COARE) bulk  
127 flux algorithm (Fairall et al. 2003) using daily QuikSCAT wind speed, TMI SST, and  
128 NCEP/NCAR reanalysis surface air temperature and specific humidity (Kalnay et al.  
129 1996). Air temperature and specific humidity were corrected for systematic biases  
130 using February 2007–November 2008 daily measurements from the RAMA mooring at  
131  $8^\circ\text{S}$ ,  $67^\circ\text{E}$  (described in section 2.2). The correction was performed by subtracting the  
132 mean difference (Feb 07 - Nov 08) between the colocated mooring and NCEP humidity  
133 (air temperature) at  $8^\circ\text{S}$ ,  $67^\circ\text{E}$  from the NCEP humidity (air temperature) at each  
134 grid point. The surface shortwave radiation (SWR) product from Zhang et al. (2004)  
135 is available during 1983–2006 on a  $2.5^\circ \times 2.5^\circ$  daily grid. To obtain a SWR product  
136 until the end of 2008, we added interannual anomalies of NOAA outgoing longwave  
137 radiation anomalies (Liebmann and Smith 1996) to the seasonal cycle of shortwave  
138 radiation product from Zhang et al. (2004). The resulting SWR product is very  
139 similar to the original product from Zhang et al. (2004), with a correlation (RMS  
140 difference) of 0.9 ( $12 \text{ W m}^{-2}$ ) for weekly values over the SCTR region. The total  
141 net surface SWR was obtained assuming an albedo of 6%. We calculate net longwave  
142 radiation emission from the Clark et al. (1974) bulk formula using daily NCEP/NCAR



143 reanalysis air temperature and humidity, TMI SST, and the SWR product described  
144 above, following the methodology of Foltz and McPhaden (2005).

145 The second net surface heat flux product (hereafter  $Flux_{OAFlux}$ ) consists of latent  
146 and sensible heat fluxes from the objectively analyzed air-sea heat fluxes (OAFflux; Yu  
147 and Weller 2007). This data set is available on a  $1^\circ \times 1^\circ$  grid for the time period  
148 1958–2006. Surface shortwave radiation is obtained from the satellite-based data set of  
149 Zhang et al. (2004), which is available during 1983–2006 on a  $2.5^\circ \times 2.5^\circ \times$  daily grid.  
150 Surface longwave radiation is obtained from the NCEP/DOE reanalysis-2 (hereafter  
151 NCEP2 reanalysis; Kanamitsu et al. 2002) on a  $2^\circ \times 2^\circ \times$  daily grid for the time period  
152 1979–2006. Each of these data sets is available at a daily resolution.

153 We use the  $Flux_{QuikSCAT}$  product along with the Coriolis MLD, mixed layer  
154 temperature, and  $\Delta T$ , and the OSCAR currents and TMI SST, to calculate the terms  
155 in the mixed layer heat budget during January 2000 through September 2008, when all  
156 data sets are available. The methodology used to compute the heat budget is described  
157 in section 3. The  $Flux_{OAFlux}$  product is used along with the drifter climatology, the de  
158 Boyer Montégut MLD, and the other data sets described in this section to assess the  
159 sensitivity of the mixed layer heat balance to different choices of surface flux, velocity,  
160 and MLD products (the sensitivity tests are discussed in detail in section 4.3.1). The  
161 combined TMI/AMSR-E SST is used for the heat budget analysis at the mooring  
162 location (described in section 3.2), and the TMI precipitation and QuikSCAT winds  
163 are used along with  $Flux_{QuikSCAT}$  to calculate surface buoyancy and wind stress forcing  
164 in the SCTR region (section 4).

## 165 **2.2 RAMA mooring**

166 To complement the global data sets described in section 2.1, we use measurements from  
167 a RAMA mooring located at 8°S, 67°E. This mooring was first deployed in January  
168 2007 during the Cirene cruise (Vialard et al. 2009) and was serviced in August 2009  
169 by R/V Marion Dufresne. Measurements, begun in mid January 2007 and continued  
170 through the present, include subsurface temperature, salinity, and velocity, as well as air  
171 temperature, relative humidity, wind velocity, shortwave radiation, and precipitation.  
172 Ocean temperature is measured at 1 m (i.e. bulk SST), 5 m, 10 m, 20 m, 40 m, 60 m,  
173 80 m, 100 m, 120 m, 140 m, 300 m, and 500 m, while salinity is measured at 1 m, 10  
174 m, 20 m, 40 m, 60 m, 100 m, and 140 m. Velocity is measured at a depth of 10 m, and  
175 meteorological measurements are made at heights of 3–4 m above sea level.

176 We use daily averaged data for the time period February 2007 – August 2008.  
177 The combination of instrument failure and vandalism resulted in gaps in some of the  
178 time series (Fig. 2). We have used vertical linear interpolation to replace the gaps in  
179 the subsurface temperature and salinity time series. The longest gaps for temperature  
180 are at depths of 20 m and 100 m and for salinity at 20 m, 40 m, and 100 m. The gaps  
181 at 100 m do not affect the calculations in our analyses since the MLD is always <60 m.  
182 We have subsampled temperature and salinity profiles from the mooring during periods  
183 when all data are available in the upper 80 m (Feb–Jul 2007 and Sep–Nov 2008) and  
184 found that the interpolated 20 m temperature is on average 0.4°C lower compared to  
185 the actual 20 m temperature, and the RMS difference between the interpolated and  
186 actual 20 m temperature is 0.5°C. For 20 m salinity, the mean bias (RMS difference)  
187 is 0.03 pss (0.10 pss), and for 40 m salinity the bias (RMS difference) is 0.01 pss  
188 (0.16 pss). These interpolation errors contribute to errors in daily MLD of  $\pm 9$  m, as

189 discussed in the Appendix. Subsurface velocity measurements are unavailable during  
 190 April–July 2007 and July–August 2008. We have filled the data gaps with OSCAR  
 191 5-day currents interpolated to a daily resolution after correcting for the record length  
 192 mean bias (OSCAR westward and southward currents are  $4 \text{ cm s}^{-1}$  and  $3 \text{ cm s}^{-1}$   
 193 larger than mooring currents). The RMS difference between 5-day averaged mooring  
 194 and OSCAR currents is  $7 \text{ cm s}^{-1}$  ( $6 \text{ cm s}^{-1}$ ) for the zonal (meridional) component.  
 195 The correlation between 5-day OSCAR and buoy currents is 0.9 for each component.

### 196 **3 Methodology**

197 To address the seasonal mixed layer heat balance in the SCTR region, we consider a  
 198 simplified version of the mixed layer heat balance (e.g., Moisan and Niiler 1998)

$$\rho c_p h \frac{\partial T}{\partial t} = q_0 - \rho c_p h \mathbf{v} \cdot \nabla T + q_{-h} + \epsilon \quad (1)$$

199 The terms in (1) represent, from left to right, mixed layer heat storage rate, surface  
 200 heat flux corrected for the penetration of shortwave radiation through the base of the  
 201 mixed layer, horizontal mixed layer heat advection, and the combination of entrainment  
 202 and vertical turbulent diffusion at the base of the mixed layer. Entrainment implicitly  
 203 contains the portion of vertical advection that is linked to water mass transformation.  
 204 Errors in the estimation of the terms in (1), and neglected physical processes, are rep-  
 205 resented by  $\epsilon$ . Here  $h$  is the mixed layer depth and  $T$  and  $\mathbf{v}$  are temperature and  
 206 velocity, respectively, vertically averaged from the surface to a depth of  $-h$ . We diag-  
 207 nose the heat budget in the SCTR region ( $50^\circ\text{E}$ – $75^\circ\text{E}$ ,  $5^\circ\text{S}$ – $12^\circ\text{S}$ ) using a combination  
 208 of satellite, atmospheric reanalysis, and Argo data and compare to the budget at the  
 209  $8^\circ\text{S}$ ,  $67^\circ\text{E}$  RAMA mooring location. The bounds for the SCTR region were chosen to

210 encompass the region with a local minimum in thermocline depth ( $<90$  m) and are  
211 consistent with those used in previous studies of SCTR variability (Xie et al. 2002;  
212 Hermes and Reason 2008; Yokoi et al. 2008).

### 213 **3.1 Satellite/Argo analysis**

214 We use weekly estimates of  $h$  and  $\partial T/\partial t$  from the Coriolis analysis to calculate mixed  
215 layer heat storage rate in the SCTR region. We regrid the TMI SST to a  $1^\circ$  resolution  
216 and calculate daily SST gradients as centered differences over a distance of  $2^\circ$ . The  
217 daily TMI SST gradients and 5-day OSCAR currents are averaged to weekly means  
218 and are used along with  $h$  to calculate horizontal mixed layer heat advection. The  
219 weekly heat storage rate and horizontal advection terms are then averaged to monthly  
220 means.

221 We use the monthly mean  $Flux_{QuikSCAT}$  data set described in section 2.1 to  
222 calculate the surface heat flux ( $q_0$ ), which consists of latent and sensible heat loss, ab-  
223 sorbed shortwave radiation, and net longwave radiation emission. Following Morel and  
224 Antoine (1994) and Sweeney et al. (2005), we model the amount of SWR penetrating  
225 through the base of the mixed layer as  $q_{pen} = 0.47q_{sfc} [V_1e^{-h/d_1} + V_2e^{-h/d_2}]$ , where  $q_{sfc}$   
226 is the surface shortwave radiation,  $d_1$  and  $d_2$  are the e-folding depths of the long visible  
227 ( $d_1$ ) and short visible and ultraviolet ( $d_2$ ) wavelengths, and  $h$  is the depth of the mixed  
228 layer in meters. The parameters  $V_1$ ,  $V_2$ ,  $d_1$ , and  $d_2$  are estimated using the monthly  
229 mean seasonal cycle of SeaWiFS chl-a concentration interpolated to a daily resolution,  
230 following Sweeney et al. (2005). In this study we use the convention that surface heat  
231 fluxes are positive when they tend to heat the mixed layer.

232 We have neglected a term in (1) that is proportional to the horizontal divergence  
233 of the vertically-averaged temperature-velocity covariance (see eq. (A19) of Moisan

234 and Niiler 1998). We found that this term is insignificant in comparison to the other  
235 terms in (1), based on monthly mean data for 2000–2004 from the Simple Ocean Data  
236 Assimilation (SODA; Carton et al. 2000). The covariance term is zero in the annual  
237 mean averaged over the SCTR region, and the magnitude of each monthly value is  
238  $<4 \text{ W m}^{-2}$ . The weakness of this term in comparison to the other terms in the heat  
239 balance is consistent with the results of Swenson and Hansen (1999) in the equatorial  
240 Pacific. We are also unable to reliably estimate  $q_{-h}$  directly and therefore estimate  
241 this term as the difference between the observed mixed layer heat storage rate and the  
242 sum of the net surface heat flux and horizontal advection.

### 243 **3.2 RAMA mooring analysis**

244 In addition to the large-scale heat budget analysis for the SCTR region, we consider  
245 the heat balance at the 8°S, 67°E RAMA mooring location. The main advantages  
246 of using the mooring data compared to Argo and satellite data sets are the smaller  
247 errors associated with the mooring surface flux measurements and the higher temporal  
248 resolution of the mooring data. Mixed layer depth and vertically averaged mixed layer  
249 temperature are calculated from buoy subsurface temperature and salinity using the  
250 criterion of a  $0.15 \text{ kg m}^{-3}$  density increase from a depth of 1 m for  $h$ . We use buoy  
251 horizontal currents at 10 m along with TMI SST gradients, calculated as centered  
252 differences over a distance of  $2^\circ$ , to calculate horizontal mixed layer heat advection.

253 Latent and sensible heat fluxes are calculated from version 3.0 of the COARE bulk  
254 flux algorithm (Fairall et al. 2003) with daily buoy estimates of SST, air temperature,  
255 relative humidity, and wind speed. Surface shortwave radiation (SWR) is available  
256 directly from the moorings, assuming an albedo of 6%. The penetrative component  
257 of SWR is calculated using the method described in section 3.1.1. We calculate net

258 longwave radiation emission (LWR) with buoy air temperature, relative humidity, SST,  
259 and SWR using the Clark et al. (1974) algorithm. The  $q_{-h}$  term is estimated as the  
260 residual in the heat balance.

## 261 **4 Results**

262 In this section we begin by examining the mean seasonal cycle in the southwestern  
263 tropical Indian Ocean. We then analyze the mixed layer heat balance in the SCTR  
264 region and at the 8°S, 67°E RAMA mooring location.

### 265 **4.1 Seasonal cycle**

266 The southwestern tropical Indian Ocean is characterized by a strong seasonal cycle of  
267 SST and surface winds. During boreal winter and spring a pool of warm SSTs extends  
268 southwestward from Indonesia to the African coast. SST exceeds 28°C throughout the  
269 SCTR region during these seasons (Fig. 1a). The southeasterly trade winds converge  
270 over the warmest SST between the equator and 10°S. Cyclonic (i.e., negative) wind  
271 stress curl and associated Ekman pumping maintain a shallow thermocline (<100 m)  
272 throughout the SCTR region in boreal winter and spring (Fig. 1c). During these  
273 seasons the MLD is generally less than 30 m throughout the SCTR region (Fig. 1e).  
274 Surface currents are dominated by the westward South Equatorial Current (SEC) to  
275 the south of 10°S and the eastward South Equatorial Countercurrent (SECC) between  
276 the equator and 5°S (Fig. 1e; Schott et al. 2009).

277 During boreal summer and fall the pool of highest SSTs is confined to the central  
278 and eastern equatorial basin, resulting in a strong northward SST gradient in the  
279 SCTR region (Fig. 1b). The southeasterly trade winds strengthen in association with  
280 the Indian summer monsoon. The thermocline remains shallow in the SCTR region

281 due to persistent negative wind stress curl and Ekman pumping, though the band of  
282 strongest negative wind stress curl has shifted farther north (Fig. 1d). The mixed  
283 layer deepens throughout most of the SCTR region during boreal summer. The SEC  
284 strengthens in the southern SCTR region in association with enhanced southeasterly  
285 trade winds, while the eastward flow associated with the SECC disappears and is  
286 replaced by southward Ekman currents (Fig. 1f; Schott et al. 2009).

## 287 **4.2 Climatological heat balance**

288 In this section we analyze the seasonal cycle of the mixed layer heat balance in the  
289 SCTR region during 2000–2008. We begin by considering the annual mean and seasonal  
290 variability of the terms in the heat balance.

291 The mixed layer heat storage rate is nearly zero averaged during the 2000-2008  
292 period, indicating that trends in SST and MLD were very small (Fig. 3a). Seasonal  
293 variability of the heat storage rate increases southward within the SCTR region due  
294 to the combination of a southward increase in the amplitude of the seasonal cycle of  
295 mixed layer temperature and a southward increase in MLD (Figs. 1, 3b).

296 The mean net surface heat flux ( $q_0$ ) is positive throughout the SCTR region,  
297 reflecting the fact that more heat is gained from solar radiation than is lost through  
298 the combination of turbulent heat fluxes and longwave radiation emission (Fig. 3c).  
299 Seasonal variability of  $q_0$  increases poleward from the  $\sim 7\text{--}9^\circ\text{S}$  latitude band, reaching  
300 a maximum at the southern edge of the SCTR region ( $12^\circ\text{S}$ ; Fig. 3d). The stronger  
301 variability in the south is due primarily to a stronger seasonal cycle of the solar zenith  
302 angle.

303 Horizontal advection tends to warm the mixed layer throughout the year in the  
304 SCTR region due to annual mean southwestward currents in the presence of a north-

305 eastward SST gradient (i. e., SST increases toward the northeast; Fig. 3e). Advection  
306 is strongest in terms of both mean and seasonal variability in the southwestern SCTR  
307 region, where westward currents are strong and there is a strong seasonal cycle of the  
308 zonal SST gradient (Figs. 1, 3e,f). Mean advection is weaker than  $q_0$  throughout the  
309 SCTR region, but its seasonal variability is comparable in magnitude.

310 The annual mean warming from the combination of  $q_0$  and horizontal advection  
311 is balanced by cooling from turbulent mixing at the base of the mixed layer ( $q_{-h}$ ; Fig.  
312 3g). The  $q_{-h}$  term reaches a minimum of  $\sim -100 \text{ W m}^{-2}$  in the southwestern SCTR  
313 region, increasing to  $\sim -45 \text{ W m}^{-2}$  in the northeast. The monthly standard deviation  
314 of  $q_{-h}$  is generally 10–20  $\text{W m}^{-2}$ , with a maximum of 40  $\text{W m}^{-2}$  in the southwestern  
315 portion of the SCTR region (Fig. 3h).

316 Next we consider the mixed layer heat balance averaged areally in the SCTR  
317 region. The SST and mixed layer heat budget components are dominated by the  
318 annual cycle (Fig. 4). SST reaches a maximum during March–April, then decreases to  
319 a minimum of  $26^\circ\text{C}$  in August. The period of strong cooling during April–July coincides  
320 with a minimum in surface and absorbed SWR in June–July. Seasonal variations of  
321 LHF and the sum of SHF and LWR are much weaker in comparison to the heat storage  
322 rate and SWR terms. The weak seasonal variability of LHF is a consequence of the out-  
323 of-phase relationship between surface wind speed and the near-surface vertical humidity  
324 gradient ( $\Delta q = q_s - q$ , where  $q_s$  is the saturation specific humidity at the SST and  $q$  is  
325 the near-surface atmospheric specific humidity): wind speed is at a maximum in boreal  
326 summer, when  $\Delta q$  is at a minimum. The minimum in  $\Delta q$  itself is driven primarily by a  
327 corresponding minimum in SST (and hence  $q_s$ ). In contrast, the seasonal amplitude of  
328  $q$  is about half as large as that of  $q_s$ . As a result, seasonal variations of LHF contribute



329 very little to seasonal variations in the net surface heat flux. The net surface heat flux  
330 instead is dominated by SWR and varies in phase with the seasonal cycle of mixed  
331 layer heat storage rate (Fig. 4c).

332 Horizontal advection provides a significant source of warming during boreal sum-  
333 mer and fall (Fig. 3). Warming from the meridional component is stronger than that  
334 from to the zonal component, due mainly to a stronger meridional SST gradient during  
335 boreal summer in comparison to the zonal gradient (Fig. 5). A maximum in MLD  
336 during boreal summer also contributes to the maximum in southwestward mixed layer  
337 heat advection.

338 Seasonal variations in the sum of the net surface heat flux and horizontal advec-  
339 tion are in phase with those of the mixed layer heat storage rate. Both terms reach  
340 minima in June and maxima in September–October. However, the sum exceeds the  
341 storage rate by 40–80 W m<sup>-2</sup> throughout the year, implying a significant contribution  
342 from  $q_{-h}$  (Fig. 4c). We expect that the annual mean  $q_{-h}$  can be attributed mainly to  
343 cooling due to the combination of entrainment and vertical turbulent diffusion. There  
344 is also a noticeable seasonal cycle in  $q_{-h}$ , with a maximum cooling in boreal summer  
345 and a minimum in winter. In the next section we explore the causes of the seasonal  
346 cycle of  $q_{-h}$  in the SCTR region.

## 347 **4.3 Residual**

### 348 **4.3.1 Data dependence**

349 It is possible that errors in the terms we estimated contribute significantly to the  
350 seasonal cycle of  $q_{-h}$ . In addition to the random errors discussed in the Appendix,  
351 there are errors related to mean biases in the parameterizations and data sets we used.  
352 In this section we therefore test the sensitivity of  $q_{-h}$  to different penetrative SWR

353 formulas and surface heat flux, velocity, and MLD products.

354 We conduct five different sensitivity analyses. For each analysis we calculate the  
355 terms in the mixed layer heat budget using the data sets and methodology described  
356 in section 3.1 except that we substitute either a different MLD (two different products  
357 are used), horizontal velocity, penetrative SWR formula, or surface heat flux. For the  
358 MLD sensitivity tests we use the de Boyer Montégut product, which is based on a  
359  $0.03 \text{ kg m}^{-3}$  density criterion, and the Coriolis temperature and salinity analyses with  
360 a  $0.25 \text{ kg m}^{-3}$  criterion instead of the original  $0.15 \text{ kg m}^{-3}$  criterion. The horizontal  
361 velocity product is the drifter-based climatology, and the net surface heat flux is the  
362  $Flux_{OAFlux}$  product, described in section 2.1. For the penetrative SWR sensitivity test  
363 we use the chlorophyll-based algorithm of Ohlmann (2003).

364 The peak-to-peak seasonal amplitude of  $q_{-h}$  varies between  $40$  and  $60 \text{ W m}^{-2}$  for  
365 each sensitivity test, and the phase is consistent, with maximum cooling in the boreal  
366 summer/fall and minimum cooling in winter/spring (Fig. 6). The largest uncertainty  
367 is associated with the choice of surface heat flux products: the  $Flux_{OAFlux}$  product  
368 results in a residual that is larger in magnitude throughout the year compared to  
369  $Flux_{QuikSCAT}$ , with a maximum difference of  $\sim 25 \text{ W m}^{-2}$  in April (black and solid red  
370 curves in Fig. 6). However, the seasonality is not significantly changed for different  
371 choices of MLD, velocity, and surface flux products. These results suggest that the  
372 seasonal cycle of  $q_{-h}$  is due mainly to unresolved physical processes and not to uncer-  
373 tainties in the data sets themselves. In the next section we therefore investigate the  
374 physical processes responsible for the seasonal cycle of  $q_{-h}$ .

### 375 4.3.2 Interpretation in terms of physical processes

376 The heat balance residual represents the sum of unresolved physical processes and the  
377 accumulation of errors from the terms we estimated directly. Among unresolved pro-  
378 cesses, the most likely candidate is vertical turbulent mixing, which involves turbulent  
379 entrainment and diffusion. In this section we consider only turbulent entrainment,  
380 recognizing that turbulent diffusion may also contribute significantly.

381 We begin by considering qualitatively the one-dimensional turbulent energy bal-  
382 ance. Entrainment ( $\partial h/\partial t > 0$ ) occurs when the combination of wind and surface  
383 buoyancy forcing results in a net generation of turbulent kinetic energy in the mixed  
384 layer (e.g., Kraus and Turner 1967). The amount of energy transferred from the atmo-  
385 sphere to the mixed layer is proportional to the sum of the cube of the friction velocity  
386 ( $u_* = \sqrt{\tau/\rho}$ , where  $\tau$  is surface wind stress magnitude and  $\rho$  is the density of seawater),  
387 and the surface buoyancy flux, defined as  $B = B_h + B_w$ , where  $B_h = \alpha c_p^{-1} Q$  is the com-  
388 ponent due to the surface heat flux and  $B_w = \beta \rho S(P - E)$  is the component due to the  
389 freshwater flux. Here  $\alpha$  is the coefficient of thermal expansion of seawater,  $c_p$  is the heat  
390 capacity,  $Q$  is the surface heat flux, and  $\beta$  is the coefficient of haline contraction. Evap-  
391 oration ( $E$ ) is calculated as  $E = LHF/(\rho L_e)$ , where  $L_e = [2.5 - 0.00236 \times SST] \times 10^6$   
392 is the latent heat of vaporization.

393 The seasonal cycle of  $q_{-h}$  agrees reasonably well with the seasonal cycles of  $u_*^3$   
394 and buoyancy forcing (Fig. 7a,b). During boreal winter and spring the buoyancy flux  
395 is positive, wind speed is low, and  $q_{-h}$  is relatively weak. During April–June there is a  
396 dramatic increase in  $u_*^3$  as the summer monsoon commences, and there is a concurrent  
397 decrease in the surface buoyancy flux that is driven mainly by a decrease in surface  
398 SWR (Figs. 4b, 7b). The  $q_{-h}$  term decreases from  $\sim -40$  W m<sup>-2</sup> in April to  $\sim -80$  W

399  $\text{m}^{-2}$  in July as  $u_*^3$  increases and the buoyancy flux decreases. The mixed layer depth  
 400 increases from 20 m in April to 50 m in September, then decreases during the fall as  
 401 the wind relaxes, suggesting that the  $q_{-h}$  term may be dominated by wind-generated  
 402 turbulent entrainment (Fig. 7d). The increase in MLD coincides with a decrease  
 403 in the distance between the base of the mixed layer and the top of the thermocline,  
 404 implying that seasonal variations in the temperature of the entrained water may also  
 405 contribute significantly. The out-of-phase relationship between  $q_{-h}$  and  $u_*^3$  and the  
 406 in-phase relationship between  $q_{-h}$  and buoyancy flux are what would be expected if  
 407 seasonal changes in  $q_{-h}$  were driven by turbulent entrainment.

408 It is also possible that seasonal changes in Ekman pumping,  $w_{ek} = \nabla \times (\frac{\tau}{\rho f})$  may  
 409 contribute to the seasonal cycle of  $q_{-h}$  through their effects on stratification and hence  
 410 the temperature of entrained water. Ekman pumping in the SCTR region undergoes  
 411 a distinct semiannual cycle, with maxima in upwelling during April and December,  
 412 in agreement with the results of Hermes and Reason (2008) and Yokoi et al. (2008).  
 413 There is also a strong annual cycle, with maximum upwelling during October–May  
 414 and a minimum during June–September (Fig. 7c). The seasonal variation of  $w_{ek}$  is  
 415 opposite of what would be expected if Ekman pumping were driving seasonal changes  
 416 in  $q_{-h}$ , however, suggesting that Ekman pumping is not a major determinant compared  
 417 to one-dimensional wind- and buoyancy-forced turbulent mixing.

418 The qualitative analysis presented in Fig. 7 provides a plausible explanation  
 419 for the observed maximum magnitude in  $q_{-h}$  during boreal summer: An increase in  
 420 wind speed and decrease in buoyancy flux during boreal spring causes a deepening of  
 421 the mixed layer and an increase in entrainment cooling. The entrainment cooling is  
 422 further enhanced during boreal summer due to the seasonal minimum in the distance

423 between the mixed layer and the thermocline. In order to quantify the entrainment  
 424 heat flux we consider the one-dimensional turbulent energy balance of Niiler and Kraus  
 425 (1977). Entrainment velocity ( $w_e \equiv H\partial h/\partial t$ , where  $H = 0$  for  $\partial h/\partial t \leq 0$  and  $H = 1$   
 426 for  $\partial h/\partial t > 0$ ) is diagnosed under the assumption that local turbulence generation is  
 427 proportional to its dissipation:

$$w_e = \frac{2mu_*^3 + \frac{h}{2} [(1+n)B_0 - (1-n)|B_0|] + \left(h - \frac{2}{\gamma}\right) J_0}{c_i^2 - s(\Delta\mathbf{v})^2} \quad (2)$$

428 Here  $u_*$  is friction velocity,  $h$  is mixed layer depth,  $B_0$  is surface buoyancy flux,  $1/\gamma$   
 429 is the shortwave extinction depth,  $J_0 \equiv \frac{g\alpha}{\rho c_p} I_0$  ( $I_0$  is the surface shortwave radiation),  
 430  $c_i^2 = \Delta b h$  ( $\Delta b = g(\rho_{-h} - \rho)$  is the buoyancy jump across the base of the mixed layer),  
 431 and  $\Delta\mathbf{v}$  is vertically averaged horizontal mixed layer velocity relative to velocity at the  
 432 base of the mixed layer. The terms represent, from left to right, turbulence generation  
 433 due to wind, surface buoyancy flux, and the penetrative component of solar radiation.  
 434 Each term is scaled by stratification and vertical velocity shear: stronger (weaker)  
 435 stratification and weaker (stronger) shear tend to reduce (enhance) the magnitude of  
 436  $w_e$ . Since we cannot reliably estimate  $\Delta\mathbf{v}$  from observations alone, we have used the  
 437 mean seasonal cycle from SODA (2000–2004) repeated for each year.

438 The constants  $m$ ,  $n$ , and  $s$  are empirically-determined proportionality factors.  
 439 Niiler and Kraus (1977) suggest that the values of  $m$  and  $n$  should be similar, while  
 440 Cronin and McPhaden (1997) estimated  $m = 0.4$ ,  $n = 0.6$ , and  $s = 0.6$  in the western  
 441 equatorial Pacific and McPhaden (1982) estimated  $m = 0.4$  at  $0^\circ$ ,  $73^\circ\text{E}$ . We have there-  
 442 fore assumed  $m = 0.4$  and  $n = s = 0.6$ . Because of large uncertainty associated with  
 443 assigning values to the proportionality factors, we expect a high degree of uncertainty  
 444 in the mean and seasonal amplitude of  $w_e$  calculated from (2). The annual mean value

445 of  $w_e$  ranges from 0.1 m to 0.6 m day<sup>-1</sup> for a parameter value ( $m = n = s$ ) ranging  
 446 from 0.2 to 0.8, and the peak-to-peak amplitude of  $w_e$  ranges from 0.5 to 1.7 m day<sup>-1</sup>.  
 447 However, the seasonal phase of  $w_e$  is the same for all reasonable parameter values,  
 448 with a distinct maximum in June and a broader minimum in boreal winter/spring.  
 449 McPhaden (1982) also found that  $w_e$  at 0°, 73°E is insensitive to the magnitudes of  $n$   
 450 and  $s$ .

451 We estimate the entrainment heat flux from (2) as  $q_{entr(NK)} = \rho c_p \Delta T w_e$ . The  
 452  $\Delta T$  term depends on the vertical temperature gradient below the mixed layer as well as  
 453 the length scale of turbulent processes as the mixed layer deepens. Values of 0.75–2°C  
 454 have been used in previous studies (i.e., Hayes et al. 1991; McPhaden 1982; Swenson  
 455 and Hansen 1999; Seager et al. 1988). Here we set  $\Delta T = T - T_{h+10}$ , where  $T_{h+10}$  is  
 456 the temperature 10 m below the base of the mixed layer. This parameterization gives  
 457  $\Delta T \simeq 1\text{--}1.5^\circ\text{C}$ , which is in the middle of the range used by previous studies.

458 The seasonal cycle of  $q_{entr(NK)}$  from (2) agrees reasonably well with the seasonal  
 459 cycle of  $q_{-h}$  calculated from the heat balance residual (Fig. 8). Both reach a minimum  
 460 in boreal summer and a maximum in the winter. There is a sharp decrease in  $q_{-h}$   
 461 and modeled entrainment during boreal spring that is due mainly to an increase in  $u_*^3$ .  
 462 The combination of the surface buoyancy flux and penetrative radiation opposes wind-  
 463 induced deepening of the mixed layer for the annual mean, but their seasonal cycles  
 464 interfere constructively (Fig. 8b). The combined buoyancy-radiation term is strongest  
 465 in boreal fall, when the surface heat flux is at a maximum and the mixed layer is thick.  
 466 The temperature jump at the base of the mixed layer ( $\Delta T$ ) is strongest in June, when  
 467 the base of the mixed layer is closest to the top of the thermocline (Fig. 7d, 8b). The  
 468 covariability of  $u_*^3$  and  $\Delta T$  results in an amplification of the seasonal cycle of  $q_{entr(NK)}$ .

469 Fig. 9 summarizes schematically the mechanisms responsible for the seasonal cycle of  
 470 entrainment in the SCTR region. We note that throughout the year the cooling from  
 471  $q_{entr(NK)}$  is  $\sim 10\text{--}50 \text{ W m}^{-2}$  weaker than from  $q_{-h}$ , suggesting that the proportionality  
 472 factors are too small or that vertical turbulent diffusion is also important.

473 An alternative to using (2) is to calculate entrainment using the observed mass  
 474 balance in the mixed layer. Following Stevenson and Niiler (1983), entrainment velocity  
 475 can be written

$$w_e = H \left( \frac{\partial h}{\partial t} + \nabla \cdot h\mathbf{v} \right) \quad (3)$$

476 Here we use weekly  $h$  and  $\mathbf{v}$  and calculate the entrainment heat flux from (3) as  
 477  $q_{entr(SN)} = \Delta T w_e$ . The entrainment heat flux from (3) exhibits a strong seasonal cycle  
 478 that varies in phase with  $q_{-h}$  and  $q_{entr(NK)}$  (Fig. 8). The strong covariability between  
 479  $q_{-h}$  and two independent estimates of entrainment suggests that the seasonal cycle of  
 480  $q_{-h}$  is driven primarily by changes in wind-generated turbulent entrainment associated  
 481 with changes in mixed layer depth.

482 The magnitude of  $q_{-h}$  exceeds the magnitude of both entrainment estimates by  
 483  $10\text{--}60 \text{ W m}^{-2}$  throughout the year, suggesting that vertical turbulent diffusion may  
 484 also contribute significantly (Fig. 8). To test this possibility, we consider the vertical  
 485 diffusion coefficient,  $K_v = -q_{diff}/(\rho_0 c_p \partial T/\partial z)$ , where  $q_{diff}$  is the difference between  
 486  $q_{-h}$  and the entrainment heat flux, and  $\partial T/\partial z$  is the average temperature gradient  
 487 between the base of the mixed layer and 10 m below the mixed layer. The annual  
 488 mean  $K_v$  for  $q_{entr(NK)}$  ( $q_{entr(SN)}$ ) is  $2.0 \text{ cm}^2 \text{ s}^{-1}$  ( $0.7 \text{ cm}^2 \text{ s}^{-1}$ ). For both entrainment  
 489 parameterizations the climatological monthly mean values of  $K_v$  are between 0.4 and  
 490  $2.5 \text{ cm}^2 \text{ s}^{-1}$ . These values generally agree with the  $0.3\text{--}2.3 \text{ cm}^2 \text{ s}^{-1}$  reported by Hayes

491 et al. (1991) for the equatorial Pacific. We note, however, that there are significant  
492 differences between the seasonal cycles in the SCTR region and in the eastern equatorial  
493 Pacific so that the values of  $K_v$  in these regions are not expected to match exactly.  
494 To estimate an upper bound on  $K_v$  we assume that the entrainment heat flux is zero  
495 and that  $q_{-h}$  is due entirely to diffusion. For this case  $K_v$  ranges from 1.0 to 2.5  $\text{cm}^2$   
496  $\text{s}^{-1}$ . These values are at the upper end of the range reported by Hayes et al. (1991)  
497 in the equatorial Pacific. This is not surprising since Hayes et al. (1991) calculated  
498 entrainment separately. The maximum values of  $K_v$  in the SCTR region are generally  
499 less than those calculated by Wang and McPhaden (1999) at  $0^\circ$ ,  $110^\circ\text{W}$  ( $K_v=1.8\text{--}3.4$   
500  $\text{cm}^2 \text{s}^{-1}$ ) and at  $0^\circ$ ,  $140^\circ\text{W}$  ( $K_v=4.0\text{--}6.5 \text{cm}^2 \text{s}^{-1}$ ). This is not surprising since Wang  
501 and McPhaden's (1999) estimates were upper bounds on  $K_v$  based on the assumption  
502 of no entrainment.

#### 503 **4.4 Heat balance at the $8^\circ\text{S}$ , $67^\circ\text{E}$ RAMA mooring location**

504 In sections 4.2 and 4.3 we analyzed the mixed layer heat budget in the SCTR region  
505 for the 2000–2008 period from a combination of satellite and in situ data sets. In this  
506 section we provide a complementary heat budget analysis at the  $8^\circ\text{S}$ ,  $67^\circ\text{E}$  RAMA  
507 mooring location, which is near the center of the SCTR region (Fig. 1). We focus  
508 on the period February 2007 through November 2008, when measurements from the  
509 mooring are available.

510 SST at the mooring location undergoes a pronounced annual cycle that is in  
511 phase with the seasonal cycle of SST in the SCTR region, though the magnitude of the  
512 annual cycle of SST is considerably weaker at the mooring location (Fig. 10a). SST  
513 has a standard deviation of  $0.7^\circ\text{C}$  at  $8^\circ\text{S}$ ,  $67^\circ\text{E}$  during 2007–2008, compared to  $1.0^\circ\text{C}$   
514 in the SCTR region. There is significant interannual variability of SST at the mooring



515 location. For example, SST during February–April 2007 is 0.5–1°C warmer compared  
516 to the same period in 2008, possibly associated with the strong positive Indian Ocean  
517 dipole event in 2006 followed by a weaker positive event in 2007 (e.g., Vinayachandran  
518 et al. 2007; Behera et al. 2008; Vialard et al. 2009). The SST anomalies during boreal  
519 winter 2007 and winter 2008 at the mooring location are consistent with those in the  
520 SCTR region during the corresponding time periods (Fig. 10a). In contrast, there are  
521 significant differences in SST at the mooring location compared to that in the SCTR  
522 region during boreal summer (Fig. 10a). SST at the mooring is warmer in summer  
523 2008 compared to summer 2007, whereas SST averaged in the SCTR region is colder  
524 during 2008.

525       Surface SWR and horizontal advection undergo pronounced seasonal cycles at  
526 the mooring location (Fig. 10b). Surface and absorbed SWR reach maxima in boreal  
527 fall and winter and sharper minima in boreal summer. Horizontal advection provides  
528 warming throughout most of the period, with a distinct maximum in boreal summer,  
529 when southward Ekman currents and the northward SST gradient are strongest (Fig.  
530 1b,f, Fig. 10b). The seasonal cycles of shortwave radiation and horizontal advection  
531 at the mooring location are similar to those averaged in the SCTR region (Figs. 4b,  
532 9b). The seasonal amplitude of zonal advection is considerably weaker at the mooring  
533 location, however, due to weaker westward surface currents and eastward SST gradients  
534 compared to other locations in the SCTR region (Fig. 1a,b). The LHF at the mooring  
535 location undergoes a strong seasonal cycle, with a minimum (corresponding to strongest  
536 latent heat loss) during boreal summer. The stronger seasonal cycle of LHF at the  
537 mooring location compared to the SCTR region as a whole is due to a weaker seasonal  
538 cycle of the vertical humidity gradient ( $\Delta q = q_s - q$ ) at the mooring location during

539 2007–08 compared to the seasonal cycle of  $\Delta q$  averaged over the SCTR region during  
 540 2000–08 (since  $\Delta q$  and wind speed vary out of phase). Additional measurements from  
 541 RAMA moorings in the southwestern tropical Indian Ocean will help to assess how  
 542 much of the difference is due to spatial variations of  $\Delta q$  versus either biases in NCEP  
 543 reanalysis  $q$  or interannual variability of  $q$ .

544 The sum of the net surface flux and horizontal advection varies in phase with  
 545 changes in the mixed layer heat storage rate during 2007–2008 (Fig. 10c). Mixed layer  
 546 heat content decreases during boreal spring and summer in association with weaker  
 547 SWR and stronger latent heat loss, and increases during the fall, when the net surface  
 548 heat flux reaches a maximum and warming from horizontal advection is strong. The  
 549 sum of the surface heat flux and horizontal advection exceeds the mixed layer heat  
 550 storage rate by  $\sim 25\text{--}75 \text{ W m}^{-2}$  throughout the period, suggesting that cooling from  
 551 vertical turbulent mixing also plays an important role in the annual mean. During 2007  
 552 there is a distinct seasonal cycle of  $q_{-h}$ , with a minimum (i. e., maximum cooling)  
 553 during boreal summer and fall and a maximum in the winter. The phasing of the  
 554 annual cycle of  $q_{-h}$  in 2007 agrees with the seasonality of  $q_{-h}$  in the SCTR region (Fig.  
 555 4c). In contrast, during 2008 there is not a clear seasonal cycle of  $q_{-h}$  at the mooring  
 556 location (Fig. 9c).

557 To investigate the causes of the seasonal cycle of  $q_{-h}$  at the mooring location  
 558 during 2007–2008 we calculate the entrainment heat flux from (2) and (3) using buoy  
 559 surface winds, heat fluxes, MLD,  $\Delta\rho$ , and  $\Delta T$ , together with TMI rainfall and OSCAR  
 560 currents. We have neglected the term proportional to  $\nabla h$  in (3) since we found that it  
 561 is insignificant for the mean seasonal cycle compared to  $h\nabla \cdot \mathbf{v}$ . The modeled  $q_{entr(NK)}$   
 562 and  $q_{entr(SN)}$  at the mooring location both reach minima in boreal summer and maxima

563 in the winter, in agreement with the phasing of entrainment in the SCTR region (Figs.  
564 8a, 11a). The  $q_{entr(NK)}$  term at the mooring location is driven primarily by seasonal  
565 changes in  $u_*^3$  and the surface buoyancy flux (Fig. 11b). The  $u_*^3$  term varies in phase  
566 with MLD, reaching a maximum in boreal summer, while the buoyancy flux varies out  
567 of phase with  $u_*^3$ , consistent with the situation in the SCTR region (Figs. 7b, 11b,c).  
568 The temperature jump at the base of the mixed layer ( $\Delta T$ ) also undergoes a noticeable  
569 seasonal cycle during 2007, reaching a maximum in boreal summer, when the mixed  
570 layer is thickest (Fig. 11c). The seasonal cycle of  $\Delta T$  is more poorly defined during  
571 2008, with a maximum in boreal spring and a local minimum in boreal summer.

572 The magnitude of the  $q_{entr(NK)}$  term is significantly smaller than that of  $q_{-h}$   
573 throughout 2007–2008 at the mooring location, consistent with the results for the  
574 SCTR region (Figs. 8, 11a). The annual mean and seasonal amplitude of  $q_{entr(SN)}$  are  
575 similar to those in the SCTR region (Fig. 11a), with maxima of 50–75 W m<sup>-2</sup> during  
576 boreal summer and minima of 10–25 W m<sup>-2</sup> during boreal winter. It is possible that  
577 the poor vertical resolution of the temperature and salinity sensors on the mooring  
578 results in an overestimate of the magnitude of  $q_{entr(SN)}$  during boreal summer 2008.  
579 Future measurements from the 8°S, 67°E mooring and other RAMA moorings will  
580 enable more detailed analyses of the seasonal mixed layer heat budget.

## 581 **5 Summary and discussion**

582 In this study we examined the seasonal mixed layer heat balance in the Seychelles-  
583 Chagos thermocline ridge (SCTR; 50°E–75°E, 5°S–12°S) region of the southwestern  
584 tropical Indian Ocean. This region is characterized by annual mean upwelling and  
585 strong seasonal cycles of SST and surface winds. It was found that seasonal variations

586 of mixed layer heat content in the SCTR region are driven by a combination of the net  
587 surface heat flux, horizontal heat advection, and vertical turbulent mixing at the base  
588 of the mixed layer, estimated as a residual in the heat balance. The net surface heat  
589 flux varies in phase with the mixed layer heat storage rate and reaches a maximum in  
590 boreal fall and winter, when surface shortwave radiation is strongest. Horizontal advec-  
591 tion is close to zero during boreal winter and spring, when SSTs in the SCTR region  
592 are highest and horizontal SST gradients are weak. During boreal summer and fall  
593 surface currents and SST gradients are stronger, resulting in significant warming from  
594 horizontal advection. Strong zonal advection is confined mainly to the western SCTR  
595 region, where the eastward SST gradient is largest. In contrast, meridional advection  
596 is strongest in the eastern SCTR region, where the northward SST gradient is most  
597 pronounced. Vertical turbulent mixing at the base of the mixed layer undergoes a sig-  
598 nificant seasonal cycle. The turbulent mixing term varies out of phase with horizontal  
599 advection, tending to cool the mixed layer most strongly during boreal summer.

600       The maximum in turbulent cooling in boreal summer coincides with a maximum  
601 in surface wind speed and a minimum in the surface buoyancy flux, suggesting that  
602 the seasonal cycle of turbulent cooling is driven primarily by local wind and buoyancy  
603 induced turbulent mixing. Consistent with this interpretation, the observed mixed  
604 layer depth increases from 50 m in May to 80 m in September. As the mixed layer  
605 deepens the distance between the base of the mixed layer and the top of the thermocline  
606 decreases and the temperature gradient at the base of the mixed layer increases, tending  
607 to decrease the temperature of water entrained into the mixed layer and enhance the  
608 magnitude of the turbulent heat flux. Two independent diagnostic mixed layer models  
609 that account for these processes reproduce the observed seasonal cycle of turbulent

610 cooling in the SCTR region. The seasonal cycle of the mixed layer heat balance in  
611 the SCTR region and its relationship to changes in mixed layer depth and thermocline  
612 depth is summarized in Fig. 12.

613 The mixed layer heat balance at a RAMA mooring located near the center of the  
614 SCTR region ( $8^{\circ}\text{S}$ ,  $67^{\circ}\text{E}$ ) is generally consistent with the climatological heat balance  
615 averaged in the SCTR region. The net surface heat flux, horizontal advection, and  
616 vertical turbulent mixing all contribute significantly to the seasonal cycle of mixed layer  
617 heat storage during 2007–2008. During 2007 the turbulent cooling term is strongest in  
618 boreal summer, when the surface wind speed is highest and mixed layer is deepening,  
619 consistent with the climatological heat balance in the SCTR region. In contrast, during  
620 2008 turbulent cooling was weaker, without a clear seasonal cycle. We found that the  
621 net surface heat flux tended to heat the mixed layer more during boreal summer and  
622 fall of 2007 compared to the same time period in 2008, consistent with the development  
623 of a positive Indian Ocean dipole event during the summer of 2007 (Vinayachandran  
624 et al., 2007; Behera et al., 2008; Vialard et al. 2009).

625 Our empirical results for the SCTR region agree well with the modeling study  
626 of Zhou et al. (2008) in the eastern SCTR region ( $6^{\circ}\text{S}$ – $7^{\circ}\text{S}$ ,  $63^{\circ}\text{E}$ – $73^{\circ}\text{E}$ ). They also  
627 show that strong warming from horizontal advection in boreal summer is balanced by  
628 entrainment cooling so that the seasonal cycle of SST is driven mainly by the surface  
629 heat flux. In contrast, the modeling results of Hermes and Reason (2008) and Yokoi et  
630 al. (2008) suggest that seasonal variations of Ekman pumping contribute significantly  
631 to the seasonal cycle of upper ocean heat content in the SCTR region. The differences  
632 are likely due to the fact that Hermes and Reason (2008) and Yokoi et al. (2008)  
633 considered the heat balance down to a fixed isotherm and depth, respectively, while

634 the Zhou et al. (2008) study and our analysis considered the heat balance in the mixed  
635 layer. Analyzing the heat balance in the mixed layer is advantageous because it allows  
636 for a direct diagnosis of SST variability.

637 SST in the SCTR region plays an important role in the climate of the Indian  
638 Ocean sector through its effects on atmospheric circulation and moisture transport.  
639 Understanding the seasonal cycle of SST is an important step toward a more complete  
640 understanding of ocean-atmosphere interactions in the tropical Indian Ocean and their  
641 effects on the Indian summer monsoon and the zonal dipole mode. The results from  
642 this study will be useful as a basis for future studies of intraseasonal and interannual  
643 SST variability in the SCTR region and to validate numerical model simulations.

## 644 **Appendix: Error estimates**

645

646 Here we describe the methodology used to estimate errors for each term in the mixed  
647 layer heat balance equation for the satellite/Argo analysis averaged in the SCTR region  
648 and for the analysis at the RAMA mooring location.

649

### 650 **Satellite/Argo**

651 Uncertainties in MLD result primarily from sampling errors associated with Argo pro-  
652 files in the SCTR region. These errors are estimated for each calendar month as the  
653 RMS difference between the monthly mean Coriolis MLD product and the de Boyer  
654 Montégut product, which uses a different MLD criterion and analysis method. Errors  
655 range from  $\pm 2$  m in November to  $\pm 12$  m in June.

656 Errors in horizontal mixed layer heat advection are calculated using errors in  
657 OSCAR currents ( $7 \text{ cm s}^{-1}$  and  $6 \text{ cm s}^{-1}$  for the zonal and meridional components,  
658 respectively, based on 5-day averaged RMS differences between buoy measurements)  
659 and TMI SST ( $0.2^\circ\text{C}$  RMS difference between daily buoy measurements). Seasonal  
660 variations in the magnitude of the errors follow the seasonal cycle of advection, with  
661 monthly errors in both advection components typically  $10\text{--}20 \text{ W m}^{-2}$  during boreal  
662 winter and  $40\text{--}50 \text{ W m}^{-2}$  during boreal summer.

663 Errors in the surface flux terms were assessed as the monthly RMS differences  
664 with values calculated from measurements at the  $8^\circ\text{S}$ ,  $67^\circ\text{E}$  mooring location during  
665 2007–2008 (16, 12, 2, and  $2 \text{ W m}^{-2}$  for SWR, LHF, LWR, and SHF, respectively).  
666 These error estimates likely represent an upper bound since the satellite-based fluxes  
667 are averaged over a  $\sim 2^\circ \times 2^\circ$  area and the mooring data are point measurements,

668 and there are errors in the mooring measurements. Errors in penetrative SWR are  
669 calculated using errors in MLD and SWR. Errors in  $q_{-h}$  are calculated as the sum of  
670 the errors for the other terms in (1), assuming the individual errors are uncorrelated  
671 in time.

672 We average each term in (1) to a monthly climatology, thereby reducing errors  
673 by 67%, assuming nine independent monthly values for each calendar month at each  
674 grid point (2000–2008). To calculate errors for quantities averaged in the SCTR region  
675 we first estimate the spatial degrees of freedom (DOF) following Smith et al. (1994).  
676 We find that there are generally  $\sim 2$ –4 DOF for each term in the SCTR region. For  
677 simplicity we therefore assume 3 DOF for all terms. Errors for area-averaged quantities  
678 are then calculated as  $\epsilon_{ave} = \sqrt{\frac{1}{N(dof)} \sum_{i=1}^N \epsilon_i^2}$ , where  $N$  is the number of grid points  
679 and  $\epsilon_i$  is the error for each grid point. Averaging spatially therefore reduces errors  
680 by  $\sim 40\%$ . Thus averaging to an area-averaged monthly climatology reduces random  
681 errors by  $\sim 80\%$  compared to individual monthly values for 2000–2008 at a single grid  
682 point. Table A1 shows typical errors for monthly mean climatologies of each term in  
683 the heat balance equation (1).

684

### 685 **RAMA mooring**

686 One of the main sources of error in the heat budget analysis at the mooring location is  
687 the estimation of MLD from the coarse vertical spacing of the buoy temperature and  
688 salinity measurements. We estimate these errors using 101 CTD profiles from WOD01  
689 in the region  $50^\circ\text{E}$ – $90^\circ\text{E}$ ,  $0^\circ$ – $20^\circ\text{S}$  following the methodology of Foltz and McPhaden  
690 (2009). We found typical errors in daily-averaged MLD of  $\pm 9$  m. Daily errors in  
691 mixed layer heat storage rate due to errors in MLD are  $27 \text{ W m}^{-2}$  on average. Er-



692 rors in mixed layer temperature are negligible compared to errors in MLD due to the  
693 vertical homogeneity of temperature in the mixed layer.

694 Errors in horizontal heat advection are calculated using errors in MLD combined  
695 with errors in horizontal currents and TMI SST. We assume an error in TMI SST  
696 of  $0.2^{\circ}\text{C}$  based on the daily RMS difference with buoy SST. Sampling error for buoy  
697 currents is  $\pm 5 \text{ cm s}^{-1}$  (Freitag et al., 2003). There is also error due to differences  
698 between velocity measured at 10 m at the mooring and the actual vertically-averaged  
699 mixed layer velocity. Using monthly data from SODA for 2000–2004 we found a RMS  
700 difference of  $3 \text{ cm s}^{-1}$  ( $2 \text{ cm s}^{-1}$ ) between 10 m and mixed layer zonal (meridional)  
701 velocity. We have therefore added these errors to the instrumental errors before com-  
702 puting horizontal advection errors. Mean daily errors in zonal (meridional) advection  
703 are  $\pm 29 \text{ W m}^{-2}$  ( $\pm 36 \text{ W m}^{-2}$ ), with the largest errors (up to  $\pm 100 \text{ W m}^{-2}$ ) during  
704 boreal summer.

705 Errors in the daily-averaged surface turbulent heat flux terms are calculated us-  
706 ing instrumental errors for air temperature, SST, wind speed, and relative humidity  
707 ( $0.2^{\circ}\text{C}$ ,  $0.02^{\circ}\text{C}$ ,  $0.3 \text{ m s}^{-1}$ , and 2.7%, respectively), together with uncertainties asso-  
708 ciated with the estimation of LHF and SHF from bulk algorithms ( $\sim 12\%$ ; Fairall et  
709 al. 1996). Instrumental errors lead to uncertainties in daily LHF and SHF at each  
710 mooring location of  $\sim \pm 15 \text{ W m}^{-2}$  and  $\sim \pm 2 \text{ W m}^{-2}$ , respectively. Errors associated  
711 with the bulk algorithms give uncertainties in LHF and SHF of  $\sim \pm 15 \text{ W m}^{-2}$  and  
712  $\sim \pm 1 \text{ W m}^{-2}$ , respectively. Total errors in daily LHF and SHF are  $\sim \pm 20 \text{ W m}^{-2}$   
713 and  $\sim \pm 3 \text{ W m}^{-2}$ , respectively, where we have assumed that instrumental and bulk  
714 algorithm errors are uncorrelated in time.

715 Errors in daily-averaged LWR are the combination of instrumental errors ( $\pm 1\%$ )

716 and errors in the LWR bulk flux algorithm. We estimate errors in the bulk algorithm as  
717 the daily RMS difference between our estimates of LWR, based on buoy measurements  
718 and the Clark et al. (1974) bulk algorithm, and direct measurements from the mooring  
719 during Jan–Feb 2007. We found an RMS difference of  $6 \text{ W m}^{-2}$ . Errors in absorbed  
720 SWR result from instrumental errors in surface SWR ( $\pm 2\%$ ; Cronin and McPhaden  
721 1997) and sampling errors in  $h$ . Total daily errors in absorbed SWR are  $\sim \pm 14 \text{ W}$   
722  $\text{m}^{-2}$ .

723 To calculate errors for monthly averages of each parameter we first calculate the  
724 integral time scale (an estimate of the time period required to gain a new degree of  
725 freedom) for each month following Davis (1976). We found values of 2–3 days for each  
726 parameter averaged over the length of each data record. For simplicity we therefore  
727 use a value of 3 days in all calculations, giving  $\sim 10$  degrees of freedom for each month.  
728 Averaging to monthly means therefore reduces random errors in daily data by a factor  
729 of about three. Table A1 shows shows typical monthly mean errors for each term in  
730 the heat balance equation (1).

731

## 732 **Acknowledgments**

733 JV is funded by Institut de Recherche pour le Développement (IRD) and did this work  
734 while visiting National Institute of Oceanography (NIO, India). PKB is supported by  
735 a Council of Scientific and Industrial Research (CSIR, India) fellowship. We thank  
736 Fabienne Gaillard for providing us the Coriolis objective analysis. We thank Clément  
737 de Boyer Montégut for making his interannual mixed layer product available to us. We  
738 are grateful to Rick Lumpkin for providing the drifter climatology and to Lisan Yu  
739 for providing the OAFflux data. TMI/AMSR-E data are produced by Remote Sensing

740 Systems and are available at [www.remss.com](http://www.remss.com). This is PMEL contribution 3443 and  
741 JISAO contribution 1767.

## 742 References

- 743 Annamalai, H., P. Liu, and S.-P. Xie, 2005: Southwest Indian Ocean SST variability:  
744 Its local effect and remote influence on Asian monsoons. *J. Climate*, **18**, 4150–  
745 4167.
- 746 Annamalai, H., H. Okajima, and M. Watanabe, 2007: Possible impact of the Indian  
747 Ocean SST on the Northern Hemisphere circulation during El Niño. *J. Climate*,  
748 **20**, 3164–3189.
- 749 Behera, S. K., J. J. Luo, and T. Yamagata, 2008: Unusual IOD event of 2007. *Geophys.*  
750 *Res. Lett.*, **35**, L14S11, doi:10.1029/2008GL034122.
- 751 Black, E., J. Slingo, and K. R. Sperber, 2003: An observational study of the rela-  
752 tionship between excessively strong short rains in coastal East Africa and Indian  
753 Ocean SST, *Mon. Weath. Rev.*, **131**, 74–94.
- 754 Bonjean, F., and G. S. E. Lagerloef, 2002: Diagnostic model and analysis of the surface  
755 currents in the tropical Pacific Ocean. *J. Phys. Oceanogr.*, **32**, 2938–2954.
- 756 Carton, J. A., X. Cao, G. Chepurin, and B. S. Giese, 2000: A Simple Ocean Data  
757 Assimilation retrospective analysis of the global ocean 1950–1995. *J. Phys.*  
758 *Oceanogr.*, **30**, 294–309.
- 759 Clark, N. E., L. Eber, R. M. Laurs, J. A. Renner, and J. F. T. Saur, 1974: Heat  
760 exchange between ocean and atmosphere in the eastern North Pacific for 1961–  
761 71. *NOAA Tech. Rep. NMRS SSRF-682*, Natl. Oceanic and Atmos. Admin.,  
762 U.S. Dep. of Commer., Washington, D.C.
- 763 Cronin, M. F., and M. J. McPhaden, 1997: The upper ocean heat balance in the west-  
764 ern equatorial Pacific warm pool during September–December 1992. *J. Geophys.*  
765 *Res.*, **102**, 8533–8553.

- 766 Davis, R. E., 1976: Predictability of sea surface temperatures and sea level pressure  
767 anomalies over the North Pacific Ocean. *J. Phys. Oceanogr.*, **6**, 249–266.
- 768 de Boyer Montégut, C. D., G. Madec, A. S. Fischer, A. Lazar, and D. Iudicone, 2004:  
769 Mixed layer depth over the global ocean: An examination of profile data and a  
770 profile-based climatology. *J. Geophys. Res.*, **109**, C12003, doi:10.1029/2004JC002378.
- 771 Duvel, J-P. and J. Vialard, 2007: Indo-Pacific sea surface temperature perturbations  
772 associated with intraseasonal oscillations of the tropical convection. *J. Climate*,  
773 **20**, 3056–3082.
- 774 Fairall, C. W., E. F. Bradley, D. P. Rogers, J. B. Edson, and G. S. Young, 1996: Bulk  
775 parameterization of air-sea fluxes for Tropical Ocean-Global Atmosphere Coupled  
776 Ocean-Atmosphere Response Experiment. *J. Geophys. Res.*, **101**, 3747–3764.
- 777 Fairall, C. W., E. F. Bradley, J. E. Hare, A. A. Grachev, and J. B. Edson, 2003:  
778 Bulk parameterization of air-sea fluxes: Updates and verification for the COARE  
779 algorithm. *J. Climate*, **16**, 571–591.
- 780 Foltz, G. R., and M. J. McPhaden, 2005: Mixed layer heat balance on intraseasonal  
781 time scales in the northwestern tropical Atlantic Ocean. *J. Climate*, **18**, 4168–  
782 4184.
- 783 Foltz, G. R., and M. J. McPhaden, 2009: Impact of barrier layer thickness on SST in  
784 the central tropical North Atlantic. *J. Climate*, **22**, 285–299.
- 785 Freitag, H. P., M. J. McPhaden, C. Meinig, and P. Plimpton, 2003: Mooring motion  
786 bias of point Doppler current meter measurements. In: Proceedings of the IEEE  
787 Seventh Working Conference on Current Measurement Technology, San Diego,  
788 CA, 13–15 March 2003, IEEE, Piscataway, NJ, 155–160.
- 789 Gaillard, F., E. Autret, V. Thierry, P. Galaup, C. Coatanoan, and T. Loubrieu, 2009:

790 Quality control of large Argo data sets. *J. Ocean. Atmos. Tech.*, **26**, 337-351.

791 Goddard, L., and N. E. Graham, 1999: Importance of the Indian Ocean for simulating  
792 rainfall anomalies over eastern and southern Africa. *J. Geophys. Res.*, **104**,  
793 19,099–19,116.

794 Han, W., D. Yuan, W. T. Liu, and D. J. Halkides, 2007: Intraseasonal variability  
795 of Indian Ocean sea surface temperature during boreal winter: Madden-Julian  
796 Oscillation versus submonthly forcing and processes. *J. Geophys. Res.*, **112**,  
797 C04001, doi:10.1029/2006JC003791.

798 Hayes, S. P., P. Chang, and M. J. McPhaden, 1991: Variability of the sea surface  
799 temperature in the eastern equatorial Pacific during 1986–88. *J. Geophys. Res.*,  
800 **96**, 10,553–10,566.

801 Hermes, J. C., and C. J. C. Reason, 2008: Annual cycle of the South Indian Ocean  
802 (Seychelles-Chagos) thermocline ridge in a regional ocean model. *J. Geophys.*  
803 *Res.*, **113**, C04035, doi:10.1029/2007JC004363.

804 Izumo, T., C. D. Montégut, J. J. Luo, S. K. Behera, S. Masson, and T. Yamagata,  
805 2008: The role of the western Arabian Sea upwelling in Indian monsoon rainfall  
806 variability. *J. Climate*, **21**, 5603–5623.

807 Joseph, P. V., J. K. Eischeid, and R. J. Pyle, 1994: Interannual variability of the onset  
808 of the Indian summer monsoon and its association with atmospheric features, El  
809 Niño, and sea surface temperature anomalies. *J. Climate*, **7**, 81–105.

810 Kalnay, E., et al., 1996: The NCEP/NCAR 40-year reanalysis project. *Bull. Am.*  
811 *Meteorol. Soc.*, **77**, 437–471.

812 Kanamitsu, M., W. Ebisuzaki, J. Woollen, S. K. Yang, J. J. Hnilo, M. Fiorino, and  
813 G. L. Potter, 2002: NCEP-DOE AMIP-II reanalysis (R-2). *Bull. Am. Meteorol.*

- 814       *Soc.*, **83**, 1631–1643.
- 815 Kraus, E. B., and J. S. Turner, 1967: A one-dimensional model of the seasonal ther-  
816       mocline II. The general theory and its consequences. *Tellus*, **19**, 98–105.
- 817 Liebmann, B., and C. A. Smith, 1996: Description of a complete (Interpolated) Out-  
818       going Longwave Radiation Dataset. *Bull. Amer. Meteor. Soc.*, **77**, 1275–1277.
- 819 Lumpkin, R., and S. L. Garzoli, 2005: Near-surface circulation in the tropical Atlantic  
820       Ocean. *Deep-Sea Res. I*, **52**, 495–518.
- 821 McPhaden, M. J., 1982: Variability in the central equatorial Indian Ocean. Part II:  
822       Oceanic heat and turbulent energy balance. *J. Mar. Res.*, **40**, 403–419.
- 823 McPhaden, M. J., K. Ando, F. Syamsudin, G. Meyers, V. S. N. Murty, Y. Ma-  
824       sumoto, M. Ravichandran, J. Vialard, L. Yu, and W. Yu, 2009: RAMA: The  
825       research moored array for African-Asian-Australian monsoon analysis and pre-  
826       diction. *Bull. Am. Meteorol. Soc.*, **90**, 459–480.
- 827 Moisan, J. R., and P. P. Niiler, 1998: The seasonal heat budget of the North Pacific:  
828       Net heat flux and heat storage rates (1950–1990). *J. Phys. Oceanogr.*, **28**, 401–  
829       421.
- 830 Morel, A., and D. Antoine, 1994: Heating rate within the upper ocean in relation to  
831       its biooptical state. *J. Phys. Oceanogr.*, **24**, 1652–1665.
- 832 Murtugudde, R., and A. J. Busalacchi, 1999: Interannual variability of the dynamics  
833       and thermodynamics of the tropical Indian Ocean. *J. Climate*, **12**, 2300–2326.
- 834 Niller, P. P., and E. B. Kraus, 1977: One-dimensional models of the upper ocean,  
835       in *Modelling and Prediction of the Upper Layers of the Ocean*, edited by E. B.  
836       Kraus, pp. 143–172, Pergamon, Tarrytown, N. Y.
- 837 Ohlmann, J. C., 2003: Ocean radiant heating in climate models. *J. Climate*, **16**,

838 1337–1351.

839 Saji, N. H., S.-P. Xie, and C.-Y. Tam, 2006: Satellite observations of intense intrasea-  
840 sonal cooling events in the tropical south Indian Ocean. *Geophys. Res. Lett.*,  
841 **33**, L14704, doi:10.1029/2006GL026525.

842 Schott F. A., S.-P. Xie, J. P. McCreary Jr., 2009: Indian Ocean circulation and climate  
843 variability. *Rev. Geophys.*, **47**, RG1002, doi:10.1029/2007RG000245.

844 Seager, R., S. E. Zebiak, and M. A. Cane, 1988: A model of the tropical Pacific sea  
845 surface temperature climatology. *J. Geophys. Res.*, **93**, 1266–1280.

846 Smith, T. M., R. W. Reynolds, and C.F. Ropelewski, 1994: Optimal averaging of  
847 seasonal sea surface temperatures and associated confidence intervals (1860-1989).  
848 *J. Climate*, **7**, 949-964.

849 Stevenson, J. W., and P. P. Niiler, 1983: Upper ocean heat budget during the Hawaii-  
850 to-Tahiti shuttle experiment. *J. Phys. Oceanogr.*, *13*, 1894–1907.

851 Sweeney, C., et al., 2005: Impacts of shortwave penetration depth on large-scale ocean  
852 circulation and heat transport. *J. Phys. Oceanogr.*, **35**, 1103–1119.

853 Swenson, M. S., and D. V. Hansen, 1999: Tropical Pacific ocean mixed layer heat  
854 budget: The Pacific cold tongue. *J. Phys. Oceanogr.*, **29**, 69–81.

855 Ummenhofer, C. C., A. Sen Gupta, M. H. England, and C. J. C. Reason, 2009:  
856 Contributors of Indian Ocean sea surface temperatures to enhanced East African  
857 rainfall. *J. Climate*, in press.

858 Vecchi, G. A., and D. E. Harrison, 2001: January 1999 Indian Ocean cooling event.  
859 *Geophys. Res. Lett.*, **28**, 3717–3720.

860 Vecchi, G. A., and D. E. Harrison, 2004: Interannual Indian rainfall variability and  
861 Indian Ocean sea surface temperature anomalies, in Wang, C., S.-P. Xie, and J. A.



- 862 Carton (eds.), *Earth's Climate: The Ocean-Atmosphere Interaction*, Geophysical  
863 Monograph 147, AGU, 247–260.
- 864 Vialard, J., G. R. Foltz, M. J. McPhaden, J. P. Duvel, and C. D. Montégut, 2008:  
865 Strong Indian Ocean sea surface temperature signals associated with the Madden-  
866 Julian Oscillation in late 2007 and early 2008. *Geophys. Res. Lett.*, **35**, L19608,  
867 doi:10.1029/2008GL035238.
- 868 Vialard, J., J-P. Duvel, M. McPhaden, P. Bouruet-Aubertot, B. Ward, E. Key, D.  
869 Bourras, R. Weller, P. Minnett, A. Weill, C. Cassou, L. Eymard, T. Fristedt,  
870 C. Basdevant, Y. Dandoneau, O. Duteil, T. Izumo, C. de Boyer Montégut, S.  
871 Masson, F. Marsac, C. Menkes, S. Kennan, 2009: Cirene: Air sea interactions in  
872 the Seychelles-Chagos thermocline ridge region. *Bull. Am. Met. Soc.*, **90**, 45–61.
- 873 Vinayachandran, P. N., J. Kurian, and C. P. Neema, 2007: Indian Ocean response to  
874 anomalous conditions in 2006. *Geophys. Res. Lett.*, **34**, L15602, doi:10.1029/2007GL030194.
- 875 Vinayachandran, P. N., and N. H. Saji, 2008: Mechanisms of South Indian Ocean in-  
876 traseasonal cooling. *Geophys. Res. Lett.*, **35**, L23607, doi:10.1029/2008GL035733.
- 877 Wang, W., and M. J. McPhaden, 1999: The surface-layer heat balance in the equatorial  
878 Pacific Ocean. Part I: Mean seasonal cycle. *J. Phys. Oceanogr.*, **29**, 1812–1831.
- 879 Xie, S.-P., H. Annamalai, F. A. Schott, and J. P. McCreary, 2002: Structure and  
880 mechanisms of south Indian Ocean climate variability. *J. Climate*, **15**, 864–878.
- 881 Yokoi, T., T. Tozuka, and T. Yamagata, 2008: Seasonal variation of the Seychelles  
882 Dome. *J. Climate*, **21**, 3740–3754.
- 883 Yu, L. S., and R. A. Weller, 2007: Objectively analyzed air-sea heat fluxes for the  
884 global ice-free oceans (1981–2005). *Bull. Am. Meteorol. Soc.*, **88**, 527–539.
- 885 Zhang, Y., W. B. Rossow, A. A. Lacis, V. Oinas, and M. I. Mishchenko, 2004: Calcu-

886 lation of radiative fluxes from the surface to top of atmosphere based on ISCCP  
887 and other global data sets: Refinements of the radiative transfer model and the  
888 input data. *J. Geophys. Res.*, **109**, D19105, doi:10.1029/2003JD004457.

889 Zhou, L., R. Murtugudde, and M. Jochum, 2008: Seasonal influence of Indonesian  
890 throughflow in the southwestern Indian Ocean. *J. Phys. Oceanogr.*, **38**, 1529–  
891 1541.

## 892 Figure Captions

893

894 **Fig. 1** Climatological (2000–2007) SST (shaded, °C) and surface wind vectors during  
895 (a) Dec–May and (b) Jun–Nov. Box encloses the SCTR region and solid black square  
896 is the position of the 8°S, 67°E RAMA mooring. (c) and (d): Same as in (a) and (b)  
897 except for depth of the 20°C isotherm (shaded, m) and wind stress curl (contours, N  
898 m<sup>-3</sup>). (e) and (f): Same as in (a) and (b) but for mixed layer depth (shaded, m) and  
899 surface current vectors.

900

901 **Fig. 2** (a) Availability of daily horizontal velocity, shortwave radiation (SWR), rela-  
902 tive humidity (RH), wind speed (WS), and air temperature (AT) from the 8°S, 67°E  
903 mooring. (b) Availability of subsurface temperature at depths between 1 m and 140  
904 m. (c) Availability of subsurface salinity between 1 m and 140 m.

905

906 **Fig. 3** Annual mean (2000–2008) (a) mixed layer heat storage rate, (c) net sur-  
907 face heat flux, (e) horizontal mixed layer heat advection, and (g) vertical heat flux  
908 at the base of the mixed layer in the SCTR region. Absolute values  $>50 \text{ W m}^{-2}$  are  
909 shaded. Right column is the same as left column except for the standard deviation of  
910 the monthly mean seasonal cycle. Values  $>25 \text{ W m}^{-2}$  are shaded.

911

912 **Fig. 4** Area-averaged seasonal cycles in the SCTR region. (a) SST. (b) Surface  
913 shortwave radiation (SWR; solid red), SWR absorbed in the mixed layer (dashed red),  
914 zonal advection (solid black), meridional advection (dashed black), the sum of net  
915 longwave radiation and sensible heat flux (green), and latent heat flux (blue). (c) Sum

916 of the net surface heat flux and horizontal advection (solid red), net surface heat flux  
917 (dashed red), mixed layer heat storage rate (black), and heat balance residual (blue).  
918 Shading in (c) represents one standard error.

919

920 **Fig. 5** Area-averaged seasonal cycles in the SCTR region. (a) Zonal (solid) and  
921 meridional (dashed) OSCAR currents. (b) Zonal (solid) and meridional (dashed) SST  
922 gradients. (c) Mixed layer depth. Shading indicates one standard error.

923

924 **Fig. 6** The  $q_{-h}$  term calculated with the default surface heat flux, mixed layer depth,  
925 velocity, and penetrative radiation terms (solid black) and with one of these terms re-  
926 placed with an alternative product: Surface heat flux (solid red), penetrative radiation  
927 formula (dashed red), mixed layer horizontal velocity (green),  $0.25 \text{ kg m}^{-3}$  criterion for  
928 MLD (solid blue), and de Boyer Montégut MLD (dashed blue).

929

930 **Fig. 7** Area-averaged seasonal cycles in the SCTR region. (a) Heat balance resid-  
931 ual. (b) Friction velocity cubed (solid) and surface buoyancy flux (dashed). (c) Ekman  
932 pumping velocity. (d) Distance between the depth of the  $20^\circ\text{C}$  isotherm and mixed  
933 layer depth (solid) and mixed layer depth (dashed).

934

935 **Fig. 8** (a) Heat balance residual ( $q_{-h}$  in eq. (1); solid line with shading indicating one  
936 standard error), entrainment based on eq. (2) (solid with squares), and entrainment  
937 based on eq. (3) (dashed). (b) Portion of entrainment from eq. (2) that is due to  
938 surface buoyancy flux (solid) and wind stress (dashed). Also shown is the temperature  
939 jump at the base of the mixed layer ( $\Delta T$ ; solid with squares). The sign of  $\Delta T$  has been

940 reversed so that larger negative values are associated with stronger entrainment cooling.

941

942 **Fig. 9** Schematic diagram illustrating the processes responsible for the seasonal cycle of entrainment in the SCTR region. Numbers are averages of surface shortwave radiation (SWR), wind speed, and the heat balance residual ( $q_{-h}$ ) during the months indicated. Positive values for SWR and  $q_{-h}$  indicate heating of the mixed layer. Horizontal dashed line represents the mixed layer depth.

947

948 **Fig. 10** Monthly SST and mixed layer heat budget at the 8°S, 67°E mooring location during February 2007 – November 2008. (a) SST (solid black) and mean seasonal cycle of SST area-averaged in the SCTR region. (b) Surface shortwave radiation (SWR; solid red), SWR absorbed in the mixed layer (dashed red), zonal advection (solid black), meridional advection (dashed black), the sum of net longwave radiation and sensible heat flux (green), and latent heat flux (blue). (c) Sum of the net surface heat flux and horizontal advection (solid red), net surface heat flux (dashed red), mixed layer heat storage rate (black), and heat balance residual (blue). Shading in (c) represents one standard error. All time series have been smoothed with a 1-2-1 running mean filter.

957

958 **Fig. 11** (a) Heat balance residual ( $q_{-h}$  in eq. (1); solid line with shading indicating one standard error), entrainment based on eq. (2) (solid with squares), and entrainment based on eq. (3) (dashed) at the 8°S, 67°E mooring location. (b) Friction velocity cubed (solid) and surface buoyancy flux (dashed). (c) Mixed layer depth (solid, with shading indicating one standard error) and temperature jump at the base of the mixed layer (dashed). All time series have been smoothed with a 1-2-1 running mean filter.

964

965 **Fig. 12** Processes contributing to the seasonal cycle of SST in the thermocline ridge  
966 region. Vertical bars represent seasonal mean values of horizontal mixed layer heat  
967 advection (green), net surface heat flux (red), and the heat balance residual (blue) in  
968  $\text{W m}^{-2}$ . Positive values indicate heating of the mixed layer. Black lines represent SST,  
969 mixed layer depth, and depth of the  $20^\circ\text{C}$  isotherm, with scales on the left.

970 **Table Caption**

971

972 **Table A1** Typical monthly mean errors for the climatological satellite/Argo analy-  
973 sis averaged in the SCTR region (left column) and for the analysis at the 8°S, 67°E  
974 RAMA mooring location (right column). Units are  $W m^{-2}$ .

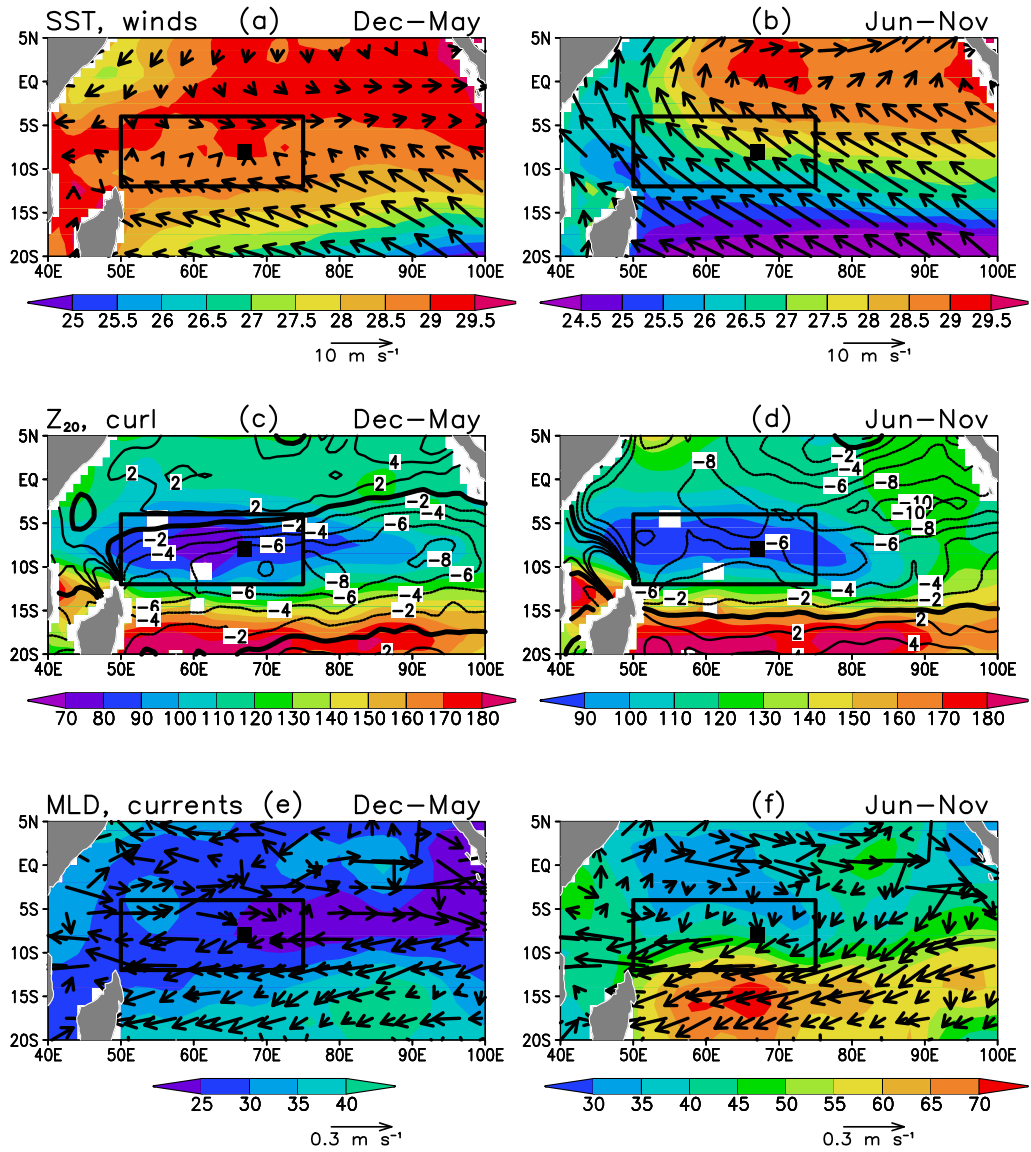


**Fig. 1** Climatological (2000–2007) SST (shaded, °C) and surface wind vectors during (a) Dec–May and (b) Jun–Nov. Box encloses the SCTR region and solid black square is the position of the 8°S, 67°E RAMA mooring. (c) and (d): Same as in (a) and (b) but for depth of the 20°C isotherm (shaded, m) and wind stress curl (contours, N m<sup>-3</sup>). (e) and (f): Same as in (a) and (b) except for mixed layer depth (shaded, m) and surface current vectors.



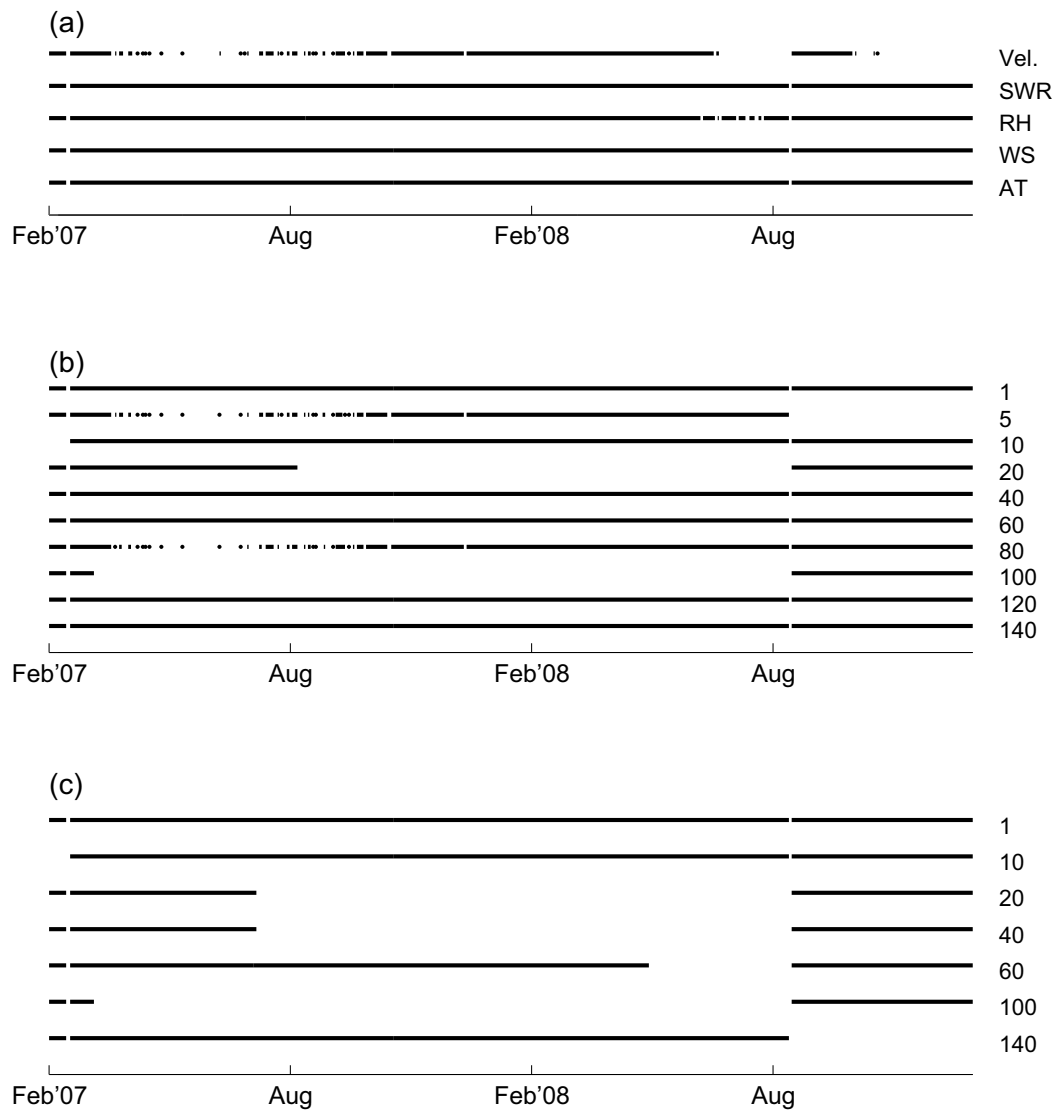


**Fig. 2** (a) Availability of daily horizontal velocity, shortwave radiation (SWR), relative humidity (RH), wind speed (WS), and air temperature (AT) from the 8°S, 67°E mooring. (b) Availability of subsurface temperature at depths between 1 m and 140 m. (c) Availability of subsurface salinity between 1 m and 140 m.

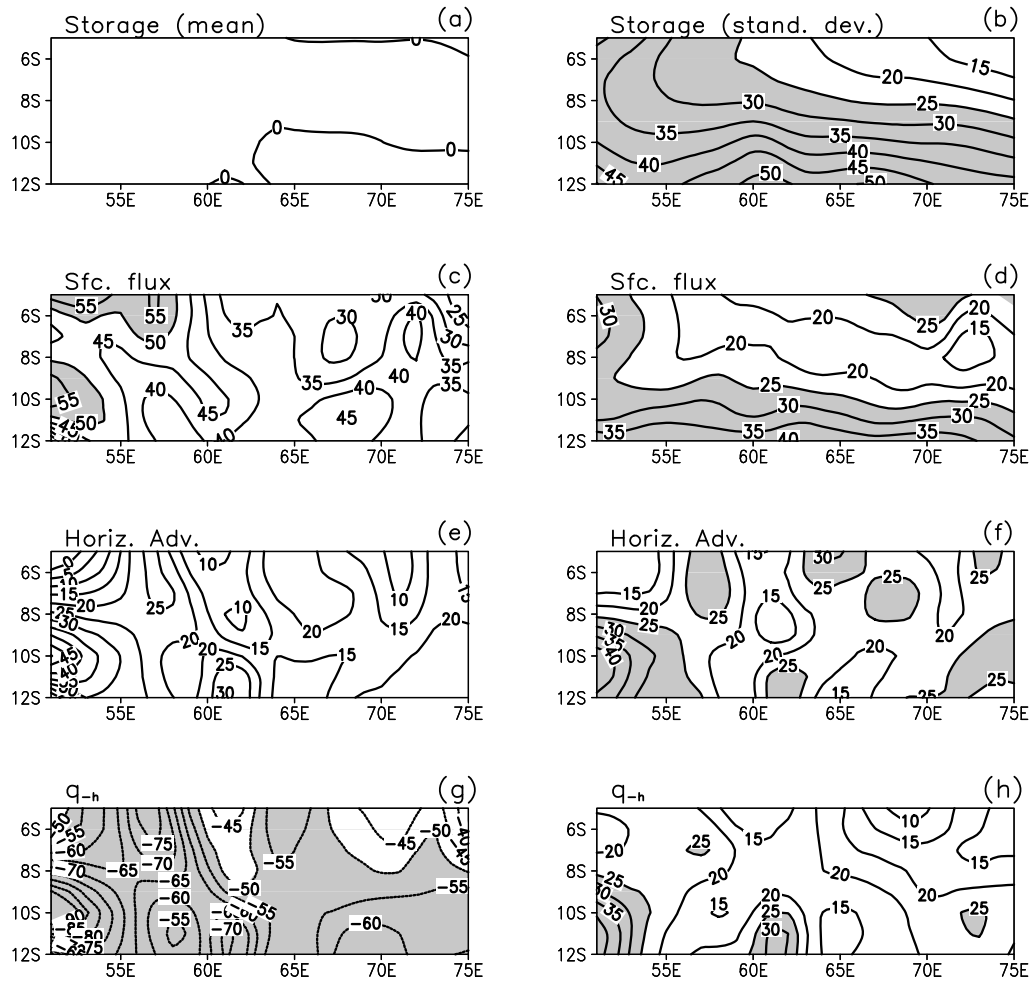


**Fig. 3** Annual mean (2000–2008) (a) mixed layer heat storage rate, (c) net surface heat flux, (e) horizontal mixed layer heat advection, and (g) vertical heat flux at the base of the mixed layer in the SCTR region. Absolute values  $>50 \text{ W m}^{-2}$  are shaded. Right column is the same as left column except for the standard deviation of the monthly mean seasonal cycle. Values  $>25 \text{ W m}^{-2}$  are shaded.

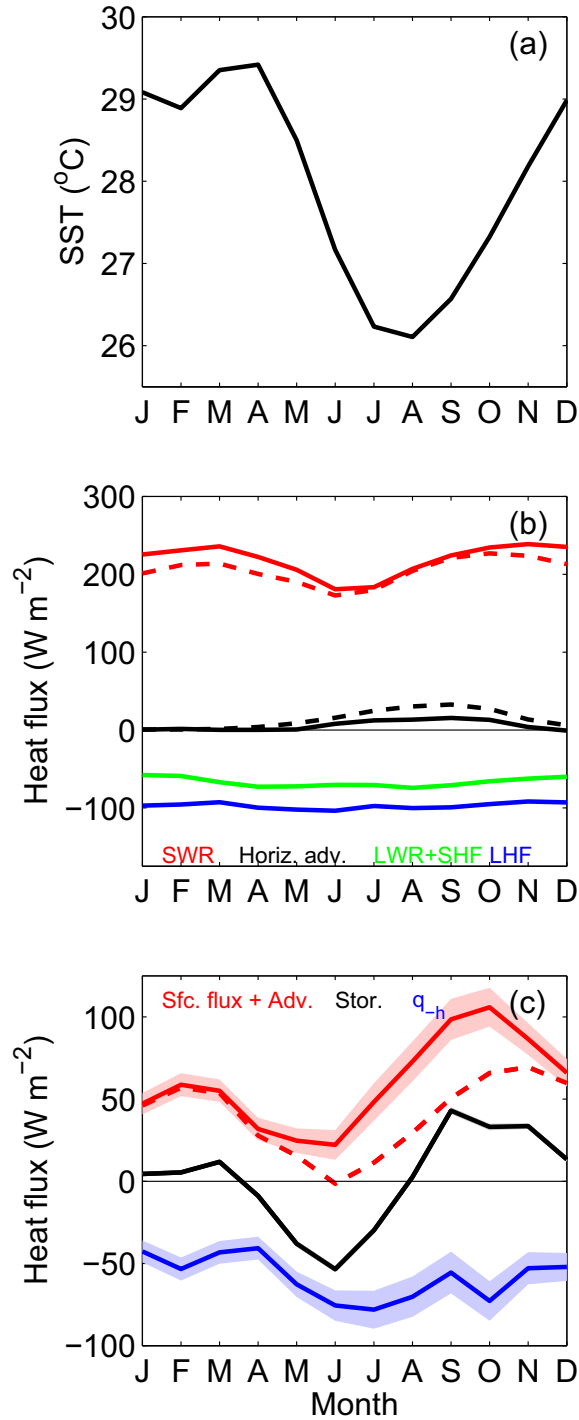


**Fig. 4** Area-averaged seasonal cycles in the SCTR region. (a) SST. (b) Surface shortwave radiation (SWR; solid red), SWR absorbed in the mixed layer (dashed red), zonal advection (solid black), meridional advection (dashed black), the sum of net longwave radiation and sensible heat flux (green), and latent heat flux (blue). (c) Sum of the net surface heat flux and horizontal advection (solid red), net surface heat flux (dashed red), mixed layer heat storage rate (black), and heat balance residual (blue). Shading in (c) represents one standard error.

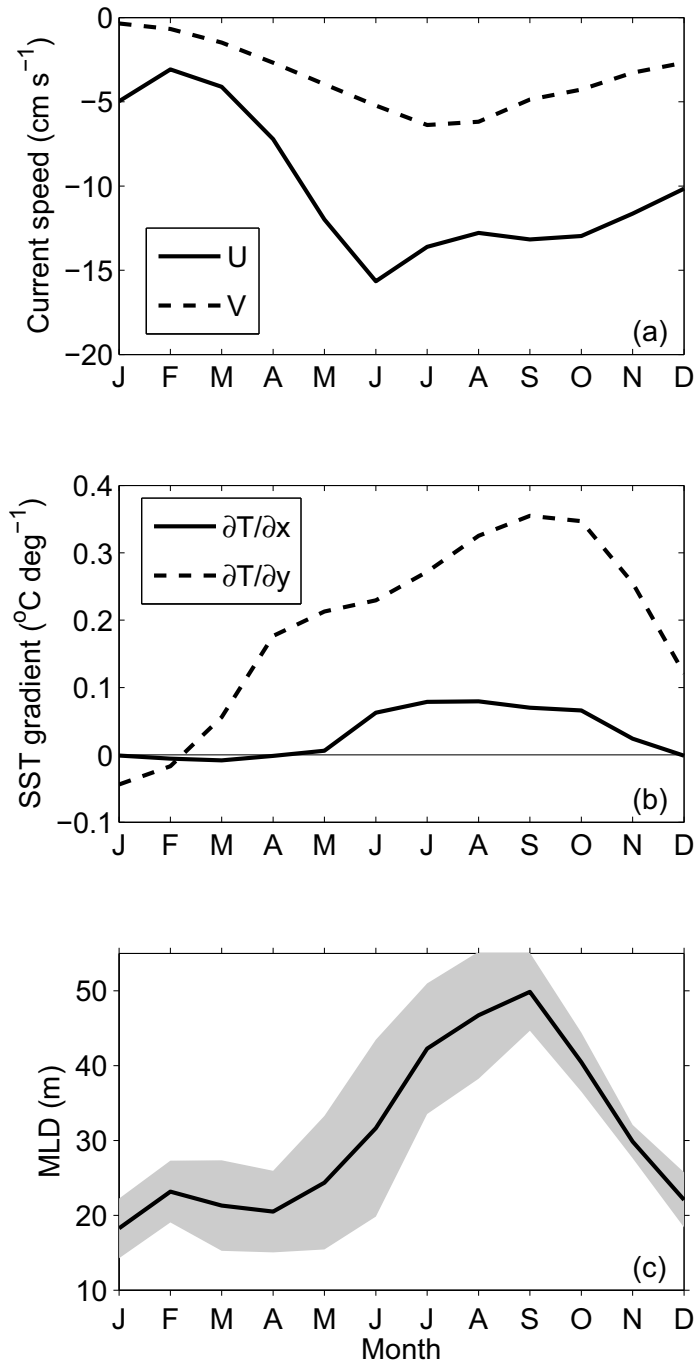


**Fig. 5** Area-averaged seasonal cycles in the SCTR region. (a) Zonal (solid) and meridional (dashed) OSCAR currents. (b) Zonal (solid) and meridional (dashed) SST gradients. (c) Mixed layer depth. Shading indicates one standard error.

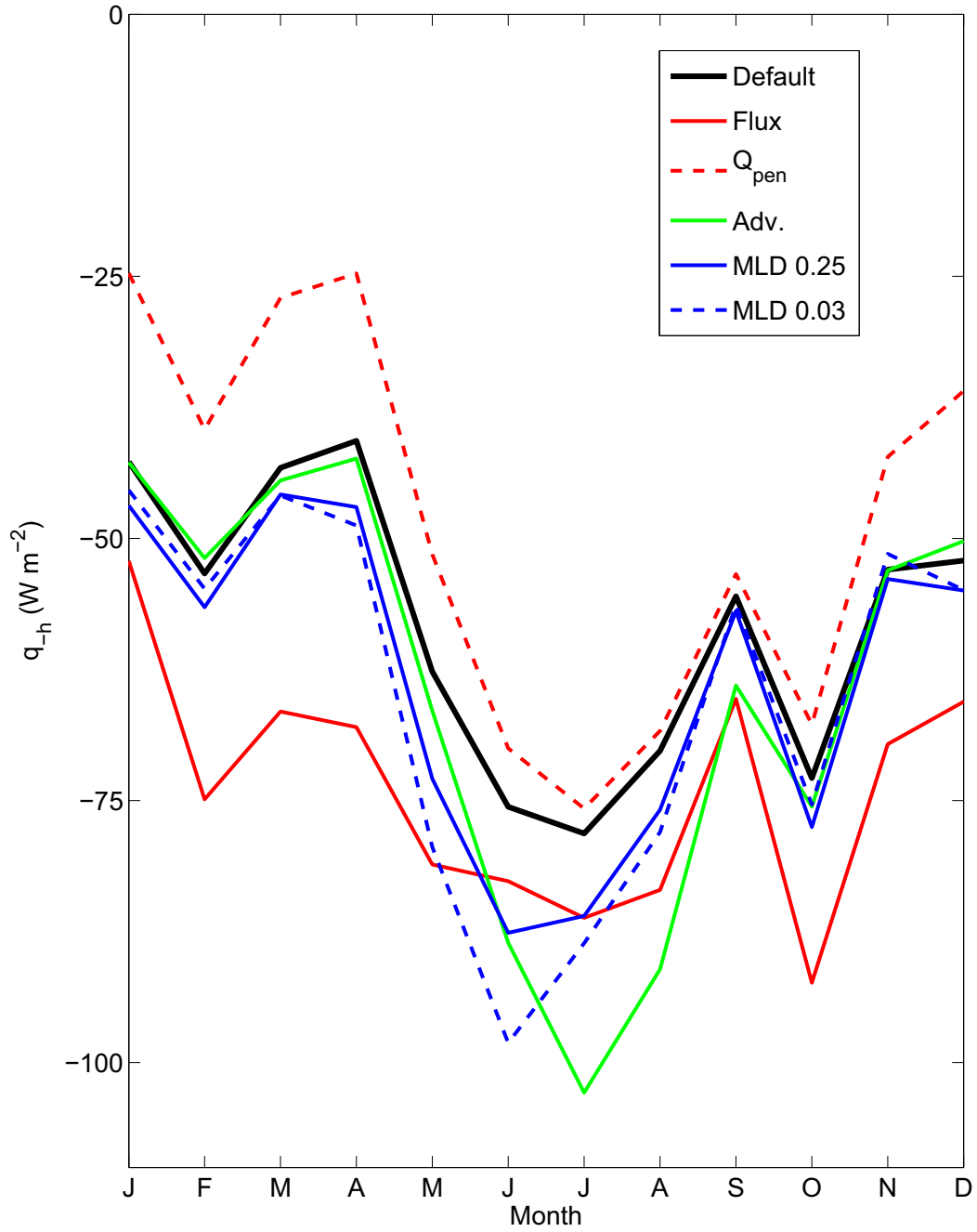


**Fig. 6** The  $q_{-h}$  term calculated with the default surface heat flux, mixed layer depth, velocity, and penetrative radiation terms (solid black) and with one of these terms replaced with an alternative product: Surface heat flux (solid red), penetrative radiation formula (dashed red), mixed layer horizontal velocity (green), 0.25 kg m<sup>-3</sup> criterion for MLD (solid blue), and de Boyer Montégut MLD (dashed blue).

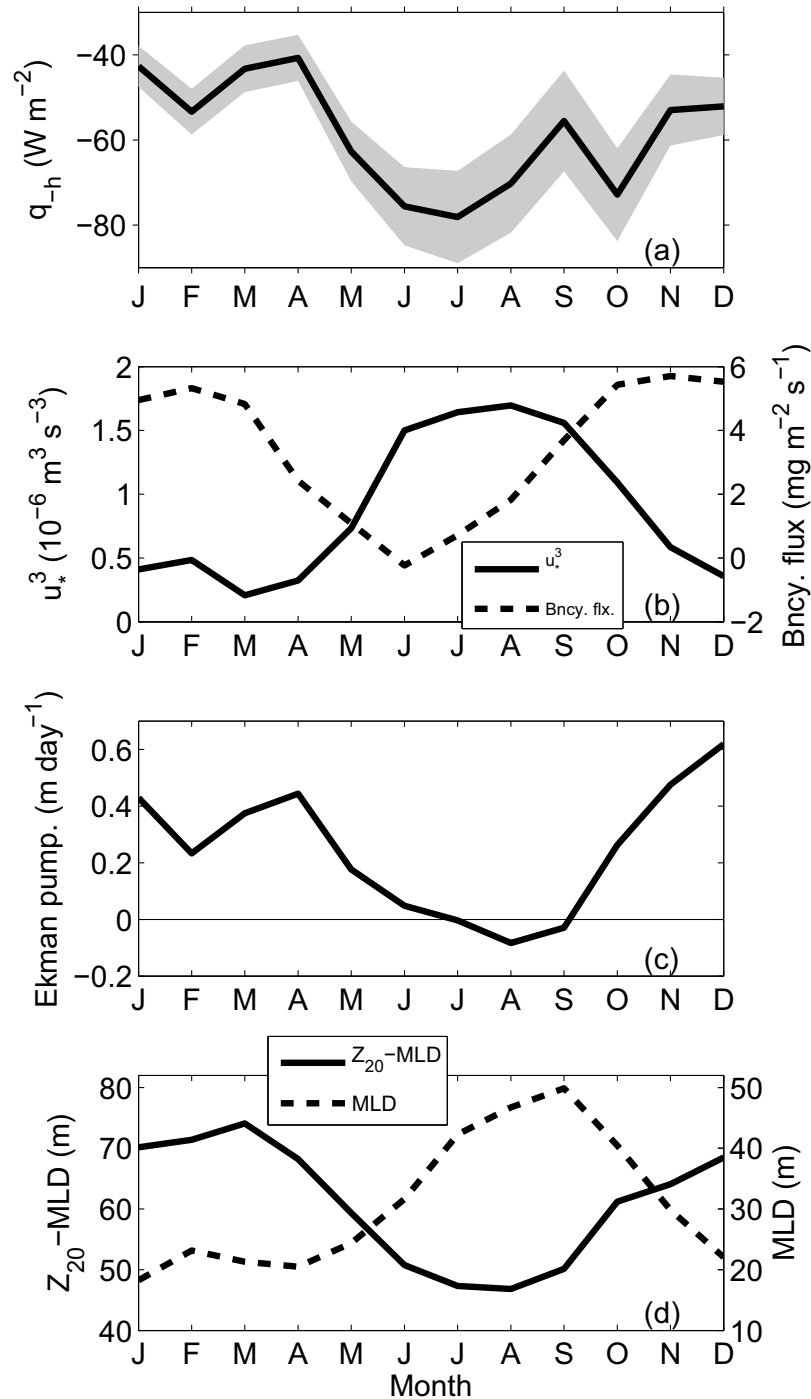


**Fig. 7** Area-averaged seasonal cycles in the SCTR region. (a) Heat balance residual. (b) Friction velocity cubed (solid) and surface buoyancy flux (dashed). (c) Ekman pumping velocity. (d) Distance between the depth of the 20°C isotherm and mixed layer depth (solid) and mixed layer depth (dashed).

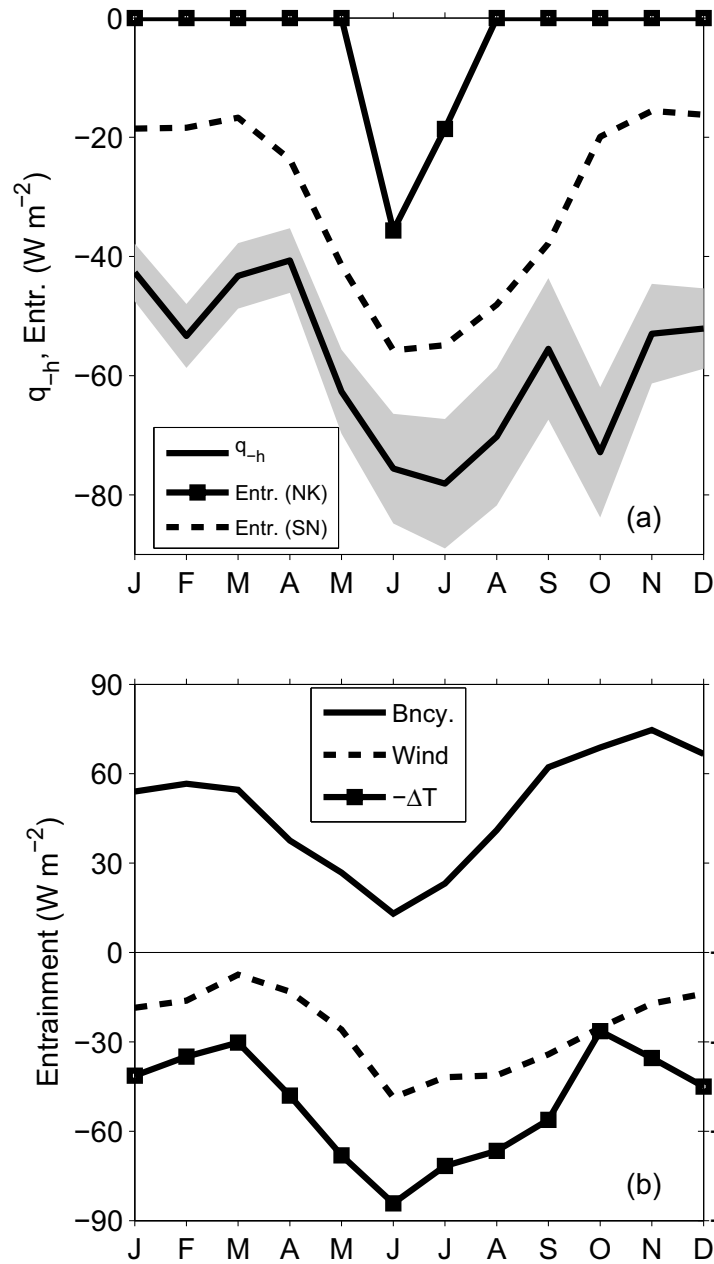
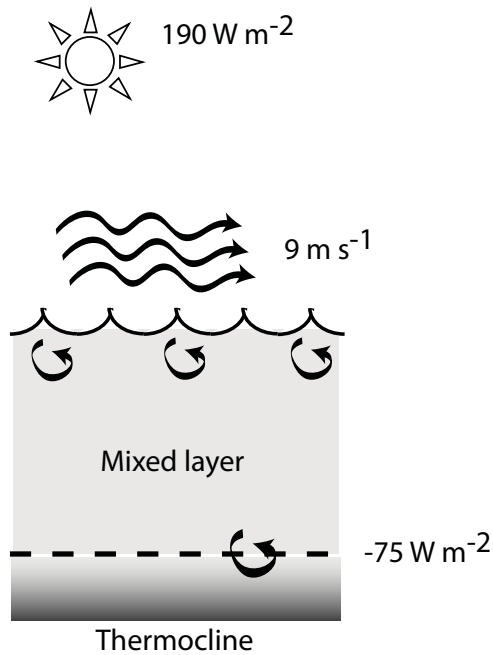


**Fig. 8** (a) Heat balance residual ( $q_{-h}$  in eq. (1); solid line with shading indicating one standard error), entrainment based on eq. (2) (solid with squares), and entrainment based on eq. (3) (dashed). (b) Portion of entrainment from eq. (2) that is due to surface buoyancy flux (solid) and wind stress (dashed). Also shown is the temperature jump at the base of the mixed layer ( $\Delta T$ ; solid with squares). The sign of  $\Delta T$  has been reversed so that larger negative values are associated with stronger entrainment cooling.

### June - August



### January - March

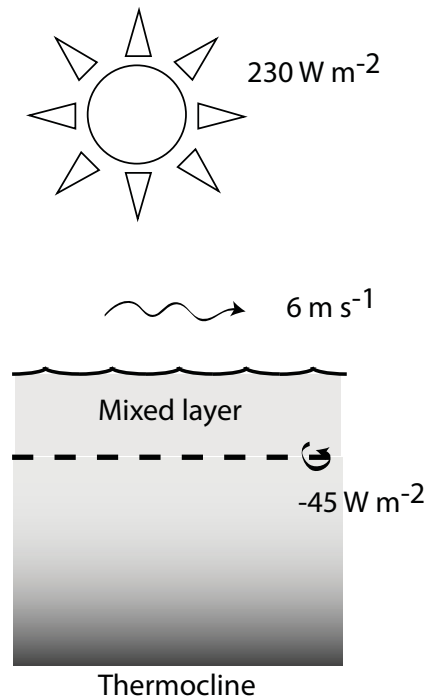


**Fig. 9** Schematic diagram illustrating the processes responsible for the seasonal cycle of entrainment in the SCTR region. Numbers are averages of surface shortwave radiation (SWR), wind speed, and the heat balance residual ( $q_{-h}$ ) during the months indicated. Positive values for SWR and  $q_{-h}$  indicate heating of the mixed layer. Horizontal dashed line represents the mixed layer depth.



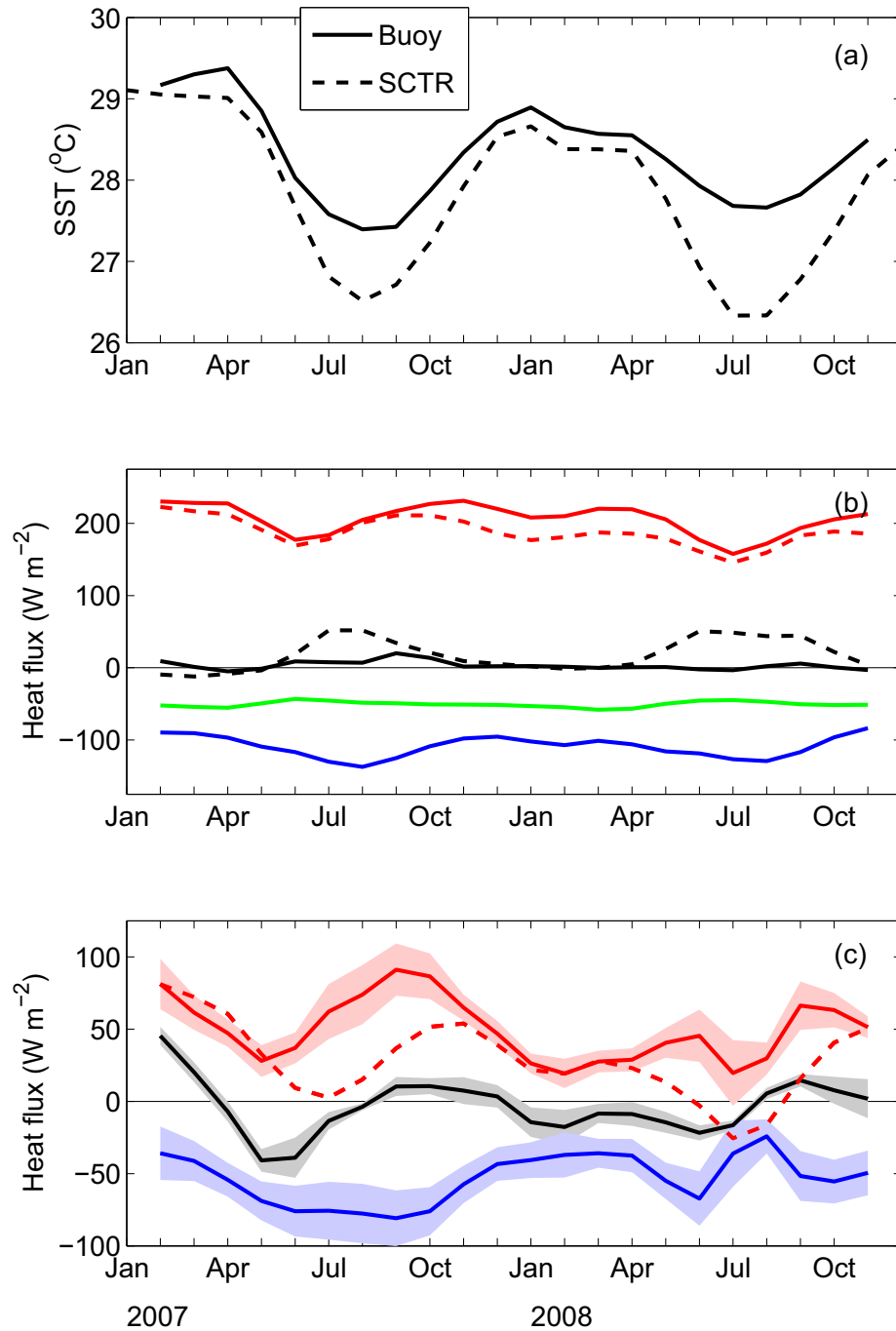


**Fig. 10** Monthly SST and mixed layer heat budget at the  $8^{\circ}\text{S}$ ,  $67^{\circ}\text{E}$  mooring location during February 2007 – November 2008. (a) SST (solid black) and mean seasonal cycle of SST area-averaged in the SCTR region. (b) Surface shortwave radiation (SWR; solid red), SWR absorbed in the mixed layer (dashed red), zonal advection (solid black), meridional advection (dashed black), the sum of net longwave radiation and sensible heat flux (green), and latent heat flux (blue). (c) Sum of the net surface heat flux and horizontal advection (solid red), net surface heat flux (dashed red), mixed layer heat storage rate (black), and heat balance residual (blue). Shading in (c) represents one standard error. All time series have been smoothed with a 1-2-1 running mean filter.

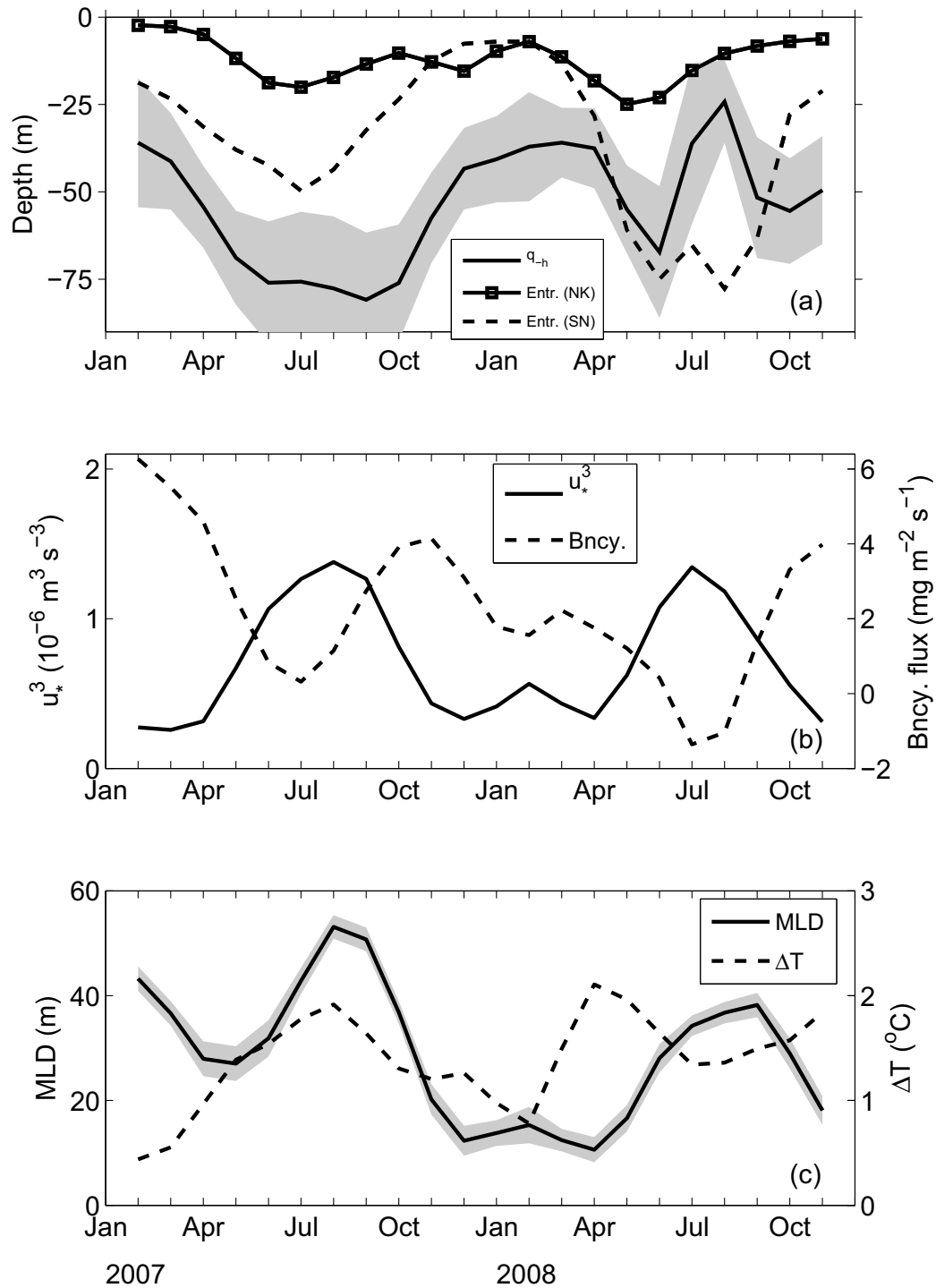


**Fig. 11** (a) Heat balance residual ( $q_{-h}$  in eq. (1); solid line with shading indicating one standard error), entrainment based on eq. (2) (solid with squares), and entrainment based on eq. (3) (dashed) at the  $8^{\circ}\text{S}$ ,  $67^{\circ}\text{E}$  mooring location. (b) Friction velocity cubed (solid) and surface buoyancy flux (dashed). (c) Mixed layer depth (solid, with shading indicating one standard error) and temperature jump at the base of the mixed layer (dashed). All time series have been smoothed with a 1-2-1 running mean filter.

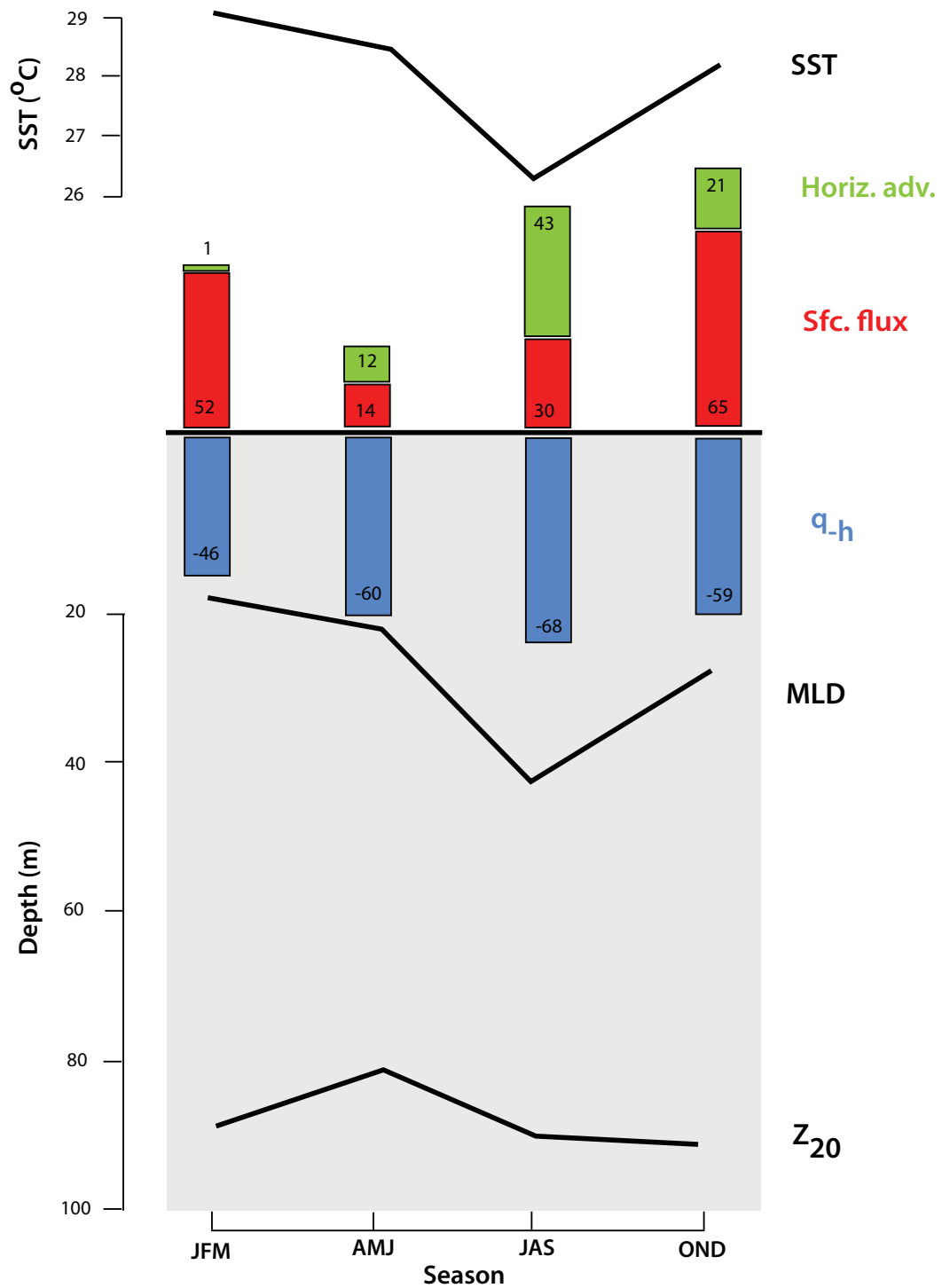


**Fig. 12** Processes contributing to the seasonal cycle of SST in the thermocline ridge region. Vertical bars represent seasonal mean values of horizontal mixed layer heat advection (green), net surface heat flux (red), and the heat balance residual (blue) in  $W m^{-2}$ . Positive values indicate heating of the mixed layer. Black lines represent SST, mixed layer depth, and depth of the 20°C isotherm, with scales on the left.

975 **Table A1** Typical monthly mean errors for the climatological satellite/Argo analysis  
 976 averaged in the SCTR region (left column) and for the analysis at the 8°S, 67°E RAMA  
 977 mooring location (right column). Units are  $W\ m^{-2}$ .

978

|              | <b>Satellite</b> | <b>RAMA</b> |
|--------------|------------------|-------------|
| Sfc. flux    | 4                | 9           |
| Horiz. adv.  | 7                | 15          |
| Heat storage | 2                | 12          |
| Residual     | 8                | 23          |

979